Politecnico di Milano
SCUOLA DI INGEGNERIA INDUSTRIALE E DELL'INFORMAZIONE
Laurea Magistrale In Ingegneria Meccanica

Complex Eigenvalue Analysis (CEA) and Design of Experiment Analysis (DOE) towards the investigation of the interaction effects of track components on rail corrugation development

Omar El Beshbichi
837590

Supervisor:
Prof. Stefano Bruni (Politecnico di Milano)

Supervisor:
Prof. Elias Kassa (NTNU)

Co-Supervisor:
Dr. Chang Wan (NTNU)

Academic Year 2016/2017

Abstract

Rail corrugation, a quasi-sinusoidal wear of the rail head, is a common issue experienced throughout the railway networks worldwide. It generally leads to high wheel-rail dynamic loads, an increased noise production and a poor ride comfort. Most commonly, rail corrugation is likely to develop on tight curved tracks. A common way to remedy rail corrugation is rail grinding, which nevertheless is an expensive and intrusive solution. Novel methods for inhibiting rail corrugation from occurrence are still being researched. A 3D finite element model for the prediction of the self-excited vibrations of the leading wheelset-rails system in a tight curved condition has been developed by using the commercial software ABAQUS. The friction coupling between the wheel and rail is taken into account. It is assumed that the creep forces between wheel and rail are saturated. The proposed model is applied to investigate the effect of several structural factors on rail corrugation. The simulation results show a strong influence of the interaction effect of the wheelset geometry and the rail gauge on rail corrugation. For a typical European wheel geometry, corrugation occurred only for a widened rail gauge. Wheels geometry is potentially an inhibitor factor at a particular rail gauge. Parameter sensitivity analysis shows that the friction coefficient is correlated linearly with the system instability and the frequency of the unstable modes of vibration.

Sommario

L'usura ondulatoria, fenomeno di rimozione periodica di materiale dalla testa dei binari, è una problematica comunemente riscontrata in tutte le reti ferroviarie. La sua formazione è spesso associata a importanti carichi dinamici scaricati sulla sala montata, un aumento complessivo del rumore emesso dal veicolo e un peggioramento del comfort dei passeggeri. L'usura ondulatoria è più comunemente associata alle zone del tracciato ferroviario a raggio stretto. La soluzione al problema adottata dalle amministrazioni ferroviarie è una semplice molatura dei binari, che tuttavia risulta un metodo costoso e invadente. Metodi precauzionali per la formazione di usura ondulatoria sono obiettivi comuni a diverse ricerche settoriali. Un modello 3D ad elementi finiti per la previsione di vibrazioni auto-eccitate della sala montata di testa di un convoglio ferroviario in corrispondenza di una condizione di curva a raggio stretto è stato sviluppato utilizzando il software commerciale ABAQUS. L'accoppiamento in frizione tra le ruote e i binari del tracciato è stato tenuto in considerazione. Le forze di attrito sono state considerate vicine alla saturazione laterale completa. Il modello proposto è stato utilizzato per investigare l'effetto di diversi parametri strutturali sulla formazione dell'usura ondulatoria. I risultati delle simulazioni evidenziano una considerevole influenza dell'effetto d'interazione tra la geometria delle ruote e lo scartamento dei binari sulla formazione dell'usura ondulatoria. Per un tipico profilo di ruota Europeo, il fenomeno in analisi si è presentato solo per uno scartamento allargato. La geometria delle ruote è quindi un potenziale parametro inibitore dell'usura ondulatoria per un particolare range di valori di scartamento. L'analisi di sensitività di singoli parametri evidenzia la correlazione lineare tra coefficiente di attrito e la stabilità del sistema e delle frequenze dei modi di vibrare instabili.

Acknowledgements

This thesis is written by me, Omar El Beshbichi, as part of my MSc studies in Mechanical Engineering at Politecnico di Milano. The work was carried at the Department of Civil and Environmental Engineering at NTNU, Norway. I would like to thank first and foremost Prof. G.X. Chen of the Tribology Research Institute at Southwest Jiaotong University, China, for giving his valuable inputs and many interesting discussions on the topic. I would like to thank also Dr. C. Wan for her help on the MBS simulations and on the revision work of the thesis. I am also grateful for the valuable support of my primary supervisor, Prof. Stefano Bruni for professional inputs and feedback. I want to thank my family: my mother, my father, and my sister, for supporting me throughout all these years.

Omar El Beshbichi, Milano, November 2017

Contents

1 Introduction **1**

1.1 Corrugation . . . 1
1.2 Aim . . . 2
1.3 Objectives . . . 2
1.4 Research Questions . . . 3
1.5 Limitations of Work . . . 3
1.6 Thesis structure . . . 3

2 Theoretical Background **5**

2.1 Corrugation . . . 5
  2.1.1 Corrugation formation mechanism . . . 5
  2.1.2 Wavelength fixing mechanisms excitation theories . . . 8
2.2 Vehicle-Track System . . . 10
  2.2.1 Railway track System . . . 10
  2.2.2 Track Dynamic Properties . . . 11
  2.2.3 Vehicle system . . . 12
2.3 Wheel-rail contact modeling . . . 13
  2.3.1 Assumptions . . . 13
  2.3.2 Main contact theories . . . 14
  2.3.3 ABAQUS FE Contact Modeling . . . 16
2.4 Wear . . . 19
2.5 Complex Eigenvalue Analysis . . . 21
  2.5.1 Complex eigenvalue extraction . . . 21
  2.5.2 Subspace projection method . . . 22

3 Method of Analysis **25**

3.1 FE Analysis . . . 25
  3.1.1 ABAQUS structure . . . 25
3.2 Dynamics . . . 26
  3.2.1 Reference track . . . 27
  3.2.2 Reference train . . . 27
  3.2.3 MBS Output . . . 27
3.3 Modeling Process . . . 29
  3.3.1 Geometries . . . 29
  3.3.2 Materials . . . 33
  3.3.3 Assembly . . . 33
  3.3.4 Interactions . . . 36
  3.3.5 Mesh . . . 39
3.4 Track Dynamic Properties . . . 40

3.4.1 Track Receptance 41
3.4.2 Track length effect on dynamic properties 41
3.5 C.E. Analysis preliminary settings 43
3.5.1 Analysis steps 43
3.5.2 Loads & Boundary conditions 44
3.6 Design of Experiments (DOE) 46
3.6.1 Parameters 47
3.6.2 DOE cases 49
3.7 Corrugation Index 49

4 Results **51**
4.1 Model Validation 53
4.2 Design of Experiments results 54
4.2.1 Effects Plots 54
4.2.2 Pareto Chart of Effects 58
4.3 Single factors effect 59
4.3.1 Friction Coefficient 60
4.3.2 Vertical RailPad Damping 60

5 Summary and Conclusions **63**
5.1 Summary 63
5.2 Conclusions 63
5.3 Limitations of the study 65
5.4 Future work 65

A Analysis input script *(2-4)* **71**

List of Figures

1.1 Corrugation of the low rail in a tight curve [5] 2

2.1 Wavelength-fixing mechanism & damage mechanism interaction schematization [6] 6
2.2 Stick slip process for a negative friction-creepage saturation relationship [11] 9
2.3 Railway schematization [15] 10
2.4 Railway track Receptance FRF [9] 12
2.5 Rail vehicle system [16] 13
2.6 Rolling contact and Coulomb's models for sliding friction [9] 15
2.7 *Hard* (a) and *Softened-exponential* (b) pressure-overclosure relationships [21] 17

3.1 ABAQUS stages for a full simulation [21] 26
3.2 High leading wheelset suspension forces: a) *Lateral forces* b) *Vertical forces*; (——) Gauge: 1435 mm, (- - -) Gauge: 1455 mm 27
3.3 Low leading wheelset suspension forces: a) *Lateral forces* b) *Vertical forces*; (——) Gauge: 1435 mm, (- - -) Gauge: 1455 mm 28
3.4 a) *Leading wheelset Yaw angle* b) *Leading wheelset Roll angle*; (——) Gauge: 1435 mm, (- - -) Gauge: 1455 mm 28
3.5 UIC60 Standard rail profile [30] 30
3.6 Transversal S-shaped European wheel profile [31] 30
3.7 Transversal SFMZ06M1 Chinese wheel profile [10] 31
3.8 JBV60 Sleeper profiles [32] 32
3.9 ORE S1002 wheel profile [33] 32
3.10 High rail sub-domains for mesh refining 34
3.11 European wheelset sub-domains for mesh refining 35
3.12 View of the assembled track model 36
3.13 Tangential contact behaviour [21] 37
3.14 Cross-shaped sleeper surface partition 38
3.15 Railpad model 38
3.16 Ballast model 39
3.17 Mesh of contact partitions at the high rail side 40
3.18 Vertical midspan track receptance functions a) Magnitude [N/mm] b) Phase [deg]; (- - -) Rail length: 4200 mm (······) Rail length: 7800 mm (——) Rail length: 11400 mm 42
3.19 Convergence of the pinned-pinned resonance frequency 43
3.20 Step flow of the analysis 44
3.21 *Black box* process model type [35] 47

4.1 Case *2-4*: Results in terms of effective damping ratios and their relative frequency. a) General results; b) Emphasis on the unstable eigenmodes 51
4.2 Case *2-4*, Mode I: Unstable modeshape 52
4.3 Case *2-4*, Mode II: Unstable modeshape 52
4.4 Validation comparison of the unstable modeshapes a) Novel model b) Reference paper model 55
4.5 Effects plots and interaction plots with respect to the wheelset design: a) Vertical ballast stiffness [MN/m]; b) Vertical railpad stiffness [MN/m]; c) Gauge [mm]; d) Wheelset design [-]. (—): Main effects; (- - -●): Wheelset design: Chinese; (- - -▲): Wheelset design: European 57
4.6 Pareto general chart of the main and interaction effects on γ; A: Rail Gauge B: Wheelset design C: Vertical Railpad stiffness D: Vertical Ballast stiffness 59
4.7 Case *2-4*: Effect of the friction coefficient μ on the effective damping ratio ●: I mode; ▲ II mode 60
4.8 Case *2-4*: Effect of the friction coefficient μ on the frequency of unstable vibration ●: I mode; ▲ II mode 60
4.9 Case *2-4*: Effect of the vertical railpad damping on the effective damping ratio ●: I mode; ▲ II mode 61

List of Tables

2.1 Classification of the main types of corrugation types according to [6] . 6

3.1 MBS steady state results 29
3.2 Unit system 33
3.3 Materials parameters 34
3.4 ABAQUS analysis steps 44
3.5 ABAQUS Loads & Boundary conditions 45
3.6 Italian gauge widening standard [38] 48
3.7 Analysis factors 48
3.8 Structural Parameters of the system 48
3.9 DOE cases 50

4.1 Case *2-4*: Unstable modes *effective damping ratios* and *frequencies* . . 52
4.2 Reference model properties 53
4.3 Validation comparison results 54
4.4 DOE results 56

Chapter 1

Introduction

1.1 Corrugation

Corrugations are quasi-sinusoidal irregularities developing in both rails and wheels. They are classified in different ways, but they are generally considered irregularities with short wavelength. The classification used by Alias [1] divides irregularities into three main categories: *corrugation*, with a wavelength between 30 and 80 mm and an amplitude of few hundreds of microns, *short waves*, with a wavelength between 150 and 300 mm and amplitudes up to 1 mm, and *long waves*, with wavelengths up to 2000 mm. In the latter case, the irregularity is generally called *Out of roundness* if owned by the wheels.

Corrugation of rail tracks has been constituting a serious issue ever since rail transportation spread as a transportation mean. Historically, the German railway system has been the first seriously affected by corrugation damage so that in the 1930s up to 46% of the Railway network was seriously damaged. For this reason, during those years *The German disease* was the typical name referring to corrugation damage [2].

Rail corrugation gives rise to very poor ride comfort, dynamic loading of both vehicle and track components and high noise levels [2]. Measurements by Vadillo et al. indicated that even in its initial phase and almost invisible, corrugation raised noise emission level by $6dB(A)$ [3].

A massive volume of research has been undertaken in this area, and a vast literature exists, from which it is clear that corrugation arises from a variety of different causes. However, despite the research, corrugation continues to be a problem whose principal means of control is *grinding* of rail. Nevertheless, grinding is regarded as a palliative rather than a cure since eventually corrugation represents. In the 1980s grinding already cost the rail industry worldwide the order of at least US$$10^8$ per annum [4].

From previous researches, it was reported that corrugation typically occurs primarily on the *low rail* in tight curves (usually curves of less than 450m radius) and in a less extent in tangential tracks at traction or braking sites [4]. Figure 1.1 depicts an example of corrugation of the low rail in tightly curved track.

Other more cost-efficient preventing solutions have been proposed during the years, which could be classified in one of the following categories: *modifications of the unsprung mass*, *modifications of the wheel-rail contact*, *modifications of the track*.

Moreover, corrugation is greatly affected by the consistency of the traffic speed at

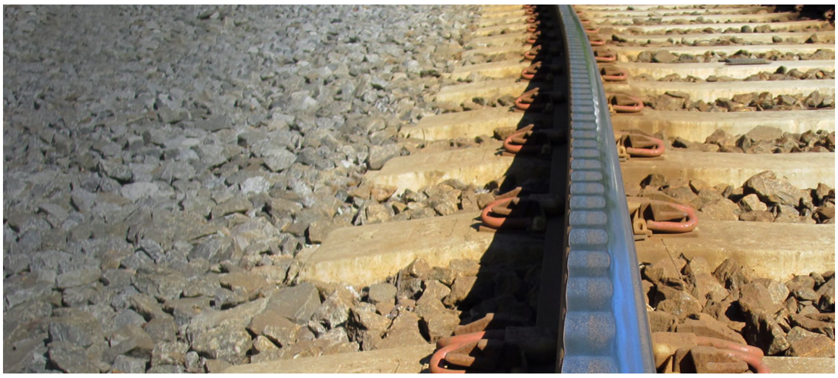

Figure 1.1: Corrugation of the low rail in a tight curve [5]

a particular rail track. A mixed traffic railway, with a mix of both vehicle type and train speed, is an ideal antidote to corrugation formation, even though this condition is generally uncommon [6]. Even though several types of rail corrugation exist, *Rutting* is the most common type of rail corrugation and occurs primarily on the low rail in tight curves.

1.2 Aim

The aim of this project is to investigate novel ways to prevent the rutting corrugation formation mechanism in tight curved tracks without the deployment of grinding as extreme solution measure, hence to examine which are the most influential factors, either structural or geometrical, on the corrugation formation mechanism and how these factors affect this phenomenon, in order to prevent it by choosing proper factors values. Moreover, a novel corrugation analysis method is here used (*complex eigenvalue analysis*) in order to qualitatively verify and compare this method with other more common corrugation analysis methods and experimental results.

1.3 Objectives

In order to achieve this aim, it will be developed a finite elements model that is able, by employing a stability analysis of the system subjected to a tight curved condition, to predict the rutting corrugation growth in the case of tight curved tracks. This approach is an application of the theory that considers as corrugation cause the instability of the wheelset-rails system caused by *self-excited vibrations* (see Chapter 2.1.2), since this approach applied to rail corrugation needs still to be further studied, and since the integration effort is smaller than in the case of more commonly used models in time domain, making this method well suitable for performing multiple cases analyses. The model will be theoretically validated by performing a comparison analysis of the results of a reference literature model. A corrugation index will be defined in the model. The model will then be used, together with a *design of experiments* procedure, to investigate the sensitivity of different factors on the corrugation growth.

1.4 Research Questions

The main research questions in the project were, therefore, the following:

1. Which are the most influencing structural parameters on rail corrugation?
2. Is there a main rutting corrugation development factor?
3. Is it possible to reduce/prevent corrugation by using proper values of these factors?
4. Does the *Complex Eigenvalue Analysis* give reliable results compared to other methods and to well assessed experimental pieces of evidence?

1.5 Limitations of Work

The master thesis contributes to 20 credits out of a total of 180 credits for the master course, therefore limitations and simplifications have to be set on the work. These simplifications are more thoroughly described in the thesis.

1.6 Thesis structure

The thesis is structured into 5 Chapters.

Chapter 2 deals with the *theoretical background* of the research.

In Section 2.1, an up to date overview of the available literature on corrugation is proposed.

Section 2.2 deals with a general summary of the components and their main properties of the structural vehicle/ track system.

Section 2.3 deals with an overview of the main analytical wheel-rail contact models, including a part on contact modeling in ABAQUS.

Section 2.4 briefly deals with wear as material removal process in the corrugation formation mechanism.

Section 2.5 deals with the theoretical formulation of the complex eigenvalue analysis, as implemented in the FE software *ABAQUS*.

Chapter 3 deals with the *methodology* involved in the very process of the research.

Section 3.1 gives a brief overview of the FE Analysis software *ABAQUS* package structure.

Section 3.2 deals with the preliminary dynamic MBS simulations for the definition of the steady-state curving condition of the system.

Section 3.3 gives an overview of the whole modeling process involved in the definition of the model used for the analysis.

Section 3.4 deals with the evaluation of the track dynamic properties through the simulation of its vertical receptance, and the definition of an optimal track length.

Section 3.5 gives an overview of the preliminary settings used in order to define correctly a complex eigenvalue analysis, both in terms of step procedures and load & boundary conditions.

Section 3.6 gives an overview of the design of experiments used for the analysis and the definition of the structural parameters of the model and of the influencing factors of study.

Chapter 4 deals with the *analysis results*.

Section 4.1 shows the validation procedure used to correlate the proposed model with the published model reference results.

Section 4.2 shows the results of the design of experiments, including common analysis charts.

Section 4.3 shows the results of the sensitivity analysis conducted for single parameters.

Chapter 5 deals with the *conclusions* of the analysis.

Section 5.1 gives a brief summary of the project work.

Section 5.2 gives an organization of the main significant results of the thesis.

Section 5.3 gives the limitations of the work.

Section 5.4 gives suggestions for future works on the subject.

Chapter 2

Theoretical Background

2.1 Corrugation

So far, the most exhaustive work that attempted to organize and describe rail corrugation is generally associated with *S. L. Grassie* and *J. Kalousek*. In particular, their review *Rail Corrugation: characteristics causes, and treatments, 1993* [6] is generally considered the first reliable work that attempted to perform such endeavor. In 2009, Grassie worked on a review article that accounted for updating the classification by taking into account new experimental and numerical pieces of evidence gathered during the previous papers. This thesis will account for these publications as literature basis on the corrugation phenomena.

In [6] a corrugation formation mechanism has been presented, which is presented in the following sections.

2.1.1 Corrugation formation mechanism

The corrugation formation mechanism is generally described by using the feedback scheme depicted in Figure 2.1.

During the working condition of the system some excitation sources that can be related to several aspects of the system (traction condition, friction condition, rail irregularity) can excite the coupled vehicle/rail track system in a more or less broad frequency range, leading to a resonance excitation of particular vibration modes of the system. The resonance of these vibration modes gives rise to a general fluctuation of all the parameters defining the contact between rail and wheel, i.e. the normal and tangential contact forces. Since the instantaneous wear rate is strictly related to the value of friction work done by the contact forces (see Chapter 2.4), a differential wear might occur, leading to a longitudinal corrugation of the rail.

These vibration modes are called *wavelength-fixing-mechanisms* since their frequencies are directly related to the corrugation wavelength on account of the above-mentioned wear mechanism. Equation (2.1.1) gives the relation between the corrugation wavelength and the frequency of the associated wavelength-fixing mechanism.

$$\lambda = \frac{\nu}{f} \tag{2.1.1}$$

where λ is the corrugation wavelength, ν is the forward vehicle speed and f the frequency of the corresponding wavelength-fixing mechanism. If the system is in

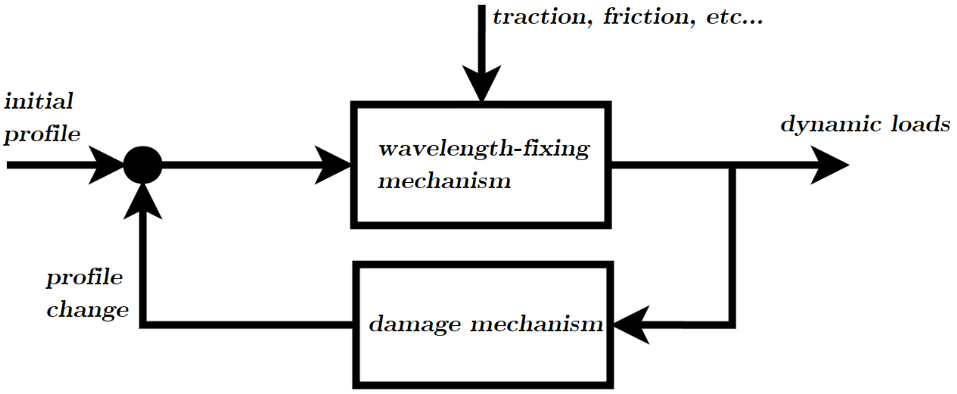

Figure 2.1: Wavelength-fixing mechanism & damage mechanism interaction schematization [6]

Table 2.1: Classification of the main types of corrugation types according to [6]

Type	Wavelength-fixing-mechanism	Damage mechanism	Frequency range [Hz]
Pinned-pinned resonance (*roaring rails*)	Pinned-pinned resonance	Wear	[400-1200]
Rutting	Second torsional resonance of driven axles	Wear	[250-400]
P2 resonance	P2 resonance	Wear/Plastic flow/Plastic bending	[50-100]

steady state, the forward train velocity won't change remarkably. Therefore, in this case, a direct relation exists between corrugation wavelength and wavelength-fixing-mechanism frequency.

The physical process involving removal of material from the rail head surface is called *damage mechanism*. The most common damage mechanism is *wear* (see Chapter 2.4). Other less common damage mechanisms could be the *plastic rail* that might occur if the rail is bent over its yield point and *plastic flow* that is a severe plastic deformation in a sub-surface layer of a few tens of microns thickness [7]. Ultimately, the wear process defines a variation of the rail head profile which in turn gives a new initial profile on the feedback loop.

Nowadays, the most common corrugation treatment is *rail grinding* of the corrugated surface of the rail head. Grinding is nevertheless an expensive and intrusive method. Another treatment for the corrugation formation is the *rail head hardening*, which clearly increases the yield strength of the rail surface. A treatment for wear induced corrugation is to use *friction modifiers* in order to control the friction curve behavior. *High friction modifiers* prevent a negative slope in the tangential contact force-tangential creepage relationship and in consequence reduce the corrugation formation [2].

Although corrugation morphology is complex to be characterized completely, evidences show that there are actually some common types of corrugation that occur more likely. They can be classified according to their wavelength-fixing mechanism and damage mechanism, as shown in Table 2.1 [8]. The next sections of the chapter will briefly list and discuss the major types of corrugation.

Pinned-pinned resonance corrugation Pinned-pinned resonance corrugation, also known as *Roaring rails*, is a common type of rail corrugation. It occurs primarily in straight lines or gentle curves, and it is also commonly associated with light axle load traffic, i.e. <20ton. [8]. This kind of corrugation is associated with the modal vibration of the rail as if a beam pinned ideally at the sleepers.

If the Euler-Bernoulli theory is used, the pinned-pinned frequency can easily be estimated. The frequency f is the same as the fundamental frequency of a simply supported beam of length L, and it is:

$$f = \frac{\omega}{2\pi} = \frac{1}{2\pi}\pi^2\sqrt{\frac{EI}{mL^4}} \tag{2.1.2}$$

where EI is the bending stiffness of the rail, m is the mass of the rail per unit length, and L is the sleeper spacing [9]. A typical frequency for a standard rail configuration (UIC60 rail with $600mm$ spacing) is around $1200Hz$. In the assumptions under the Euler-Bernoulli theory, the cross section is always perpendicular to the bending line. Moreover, no shear deformation is allowed. Therefore, if the span length L is of the same order of magnitude of the beam height the Euler-Bernoulli model gets too rigid, which is actually the case of a rail track. The frequency associated with Eq.2.1.2 is usually 20-25% higher than the real pinned-pinned resonance frequency [9].

Rutting corrugation

Rutting corrugation is another common type of corrugation and occurs primarily on the inside rail in curves when the traction ratio (ratio between the tangential to normal force) on one wheel (usually the outer wheel of the leading wheelset) is close to the friction limit, so that it drives a roll-slip unstable oscillation. To less extent it can also occur in straight lines where the traction/braking forces are sufficiently high. It is usually associated with the second torsional resonance of the driven wheelsets [4]. The frequency of the second torsional resonance is usually around $250 - 400Hz$. Rutting of the inside rail in curves is by far the most common corrugation mechanism.

P2 resonance corrugation

P2 resonance is associated by definition to the resonance of the unsprung masses on the track stiffness. It's the corrugation type with the longest wavelength: the typical frequency range is $50 - 100Hz$ depending on the structural properties of the track. Since this resonance frequency range is similar to the frequency range of the first torsional mode of the wheelset, in the first place P2 resonance was considered only a secondary phenomenon that might contribute to the corrugation formation by exciting other modes. There are several cases of P2 resonance where the damage mechanism is different: in *heavy haul corrugation* the damage mechanism is *plastic flow*, associated to high axle loads, and *light rail corrugation* where the damage mechanism is *plastic bending*, associated with rails with low bending strength.

2.1.2 Wavelength fixing mechanisms excitation theories

There are two main schools of thought about the theory associated with the main wavelength fixing mechanism excitation in railways.

- Longitudinal rail head irregularity
- Instability of the wheel-rail system: *Roll-Slip vibrations*
- Instability of the wheel-rail system: *Self-excited vibrations*

Longitudinal railhead irregularity mechanism

In this school of thought, the corrugation formation in the rail head is considered due to an excitation of wavelength fixing mechanisms due to an initial longitudinal irregularity of the rail, always present after the manufacturing process. This theory has been the most studied in the literature, mainly by means of time-domain numerical models [10]. This approach is not free of limitations since it only considers the vertical wheel-rail dynamics usually without considering the deformability of the wheelset and therefore is usually suitable for modeling corrugation types typically occurring at straight lines where the wavelength fixing mechanism is usually associated with modes of vibration of the rail, e.g pinned-pinned corrugation.

Instability of the wheel-rail system mechanism

The second and third theories consider as main cause of excitation of wavelength fixing mechanisms the instability of the wheel-rail system in particular situations. The researchers who accept this school of thought are so far less than those who accept the first school of thought, but its impact has been steadily increasing [10]. In the literature, the instability of the wheel-rail system has been considered caused by the behavior of the contact interaction when the creep forces are near saturation, i.e. when the maximum amount of tangential contact force available μN is reached.

Roll-slip In this case, instability of the wheel-rail system is considered related to the unstable stick-slip mechanism between wheel and rail. Stick-slip interaction is more properly defined as *roll-slip* mechanism in the particular application of a rolling wheel contact interaction with a rail. Roll-slip is a periodic passage of the contact condition from rolling to slipping and vice-versa. This phenomenon will make the overall creepage, as well as the creep forces, oscillate at the same frequency, thus becoming a wavelength fixing mechanism from the point of view of the corrugation formation.

According to the available literature, there are two main mechanisms for the roll-slip initiation.

- *Periodic variation of the normal contact force between wheel and rail near saturation*
- *Negative slope of the friction-creepage relationship after saturation*

In the first mechanism, according to [12], the main causes of corrugation formation are the large creepage between wheel and rail, almost near saturation, and a periodical change of the vertical contact force between wheel and rail. The variation of vertical contact force can be induced by the passing over the longitudinal irregularity on the

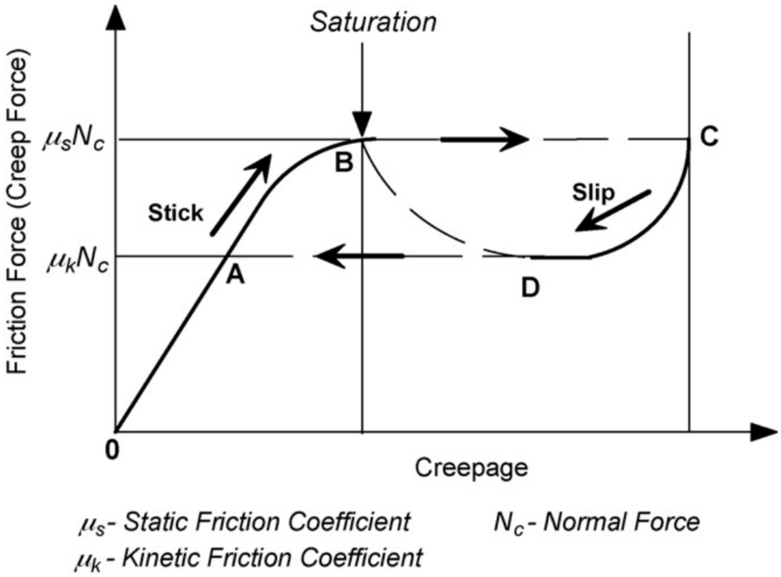
Saturation
Friction Force (Creep Force)
$\mu_s N_c$
$\mu_k N_c$
Stick
Slip
A
B
C
D
0
Creepage
μ_s - Static Friction Coefficient
N_c - Normal Force
μ_k - Kinetic Friction Coefficient

Figure 2.2: Stick slip process for a negative friction-creepage saturation relationship [11]

rail, while the high creep forces are associated generally to severe curving conditions. During the reduction periods of the wheel vertical load, the wheel will slip because the maximum creep force available will not be any more able to accommodate the external tangential loads applied to the wheel. In the same way, during the increasing periods of the wheel vertical load, the wheel will stick (roll) again when the maximum creep force available will be enough to compensate the external tangential loads.

In the second mechanism instead, according to [11], the main cause of corrugation formation is the negative friction slope after saturation in the creep force-creepage relationship.

Figure 2.2 depicts the friction force-creepage relationship and a scheme of the stick-slip interaction process. When the creepage is large enough to saturate completely the contact, the wheel will slip on the rail. The reduction of the friction force between wheel and rail sometimes triggers the releasing of the accumulated elastic energy restrained in the wheelset and rail flexibilities, reducing the tangential forces and making the wheel stick again to the rail [11].

Self-excited vibrations In this case, according to [10], the instability of the wheel-rail system is considered related to friction-induced dynamic instabilities of the system, i.e. *Self-excited vibrations.* From this point of view, the contact forces field present on the system is not conservative. Therefore, when the magnitude of the creep forces is maximum, namely when the contact is saturated, the system might experience dynamically unstable modes of vibration. In other words, the contact forces lead to an asymmetric stiffness matrix of the system and hence the potential instability occurrence. This theory, because of its novel conception, still hasn't been validated through a thorough experimental survey. However, in [10] Chen et al. studied rail corrugation by using two different methods, namely the *self-excited vibration* theory and a *transient-dynamic analysis*, showing a surprisingly good match between

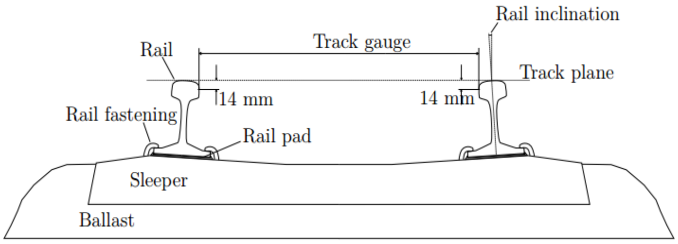

Figure 2.3: Railway schematization [15]

the results obtained. Research on this topic is still been performing. A wide employed numerical method used to study dynamic instability of mechanical systems in the frequency domain by means of a FE model is the *Complex Eigenvalue Analysis* (see Chapter 2.5).

2.2 Vehicle-Track System

The coupled railway-vehicle system is complex and composed of several structural components. In this chapter, a brief description of the main components, parameters, and properties of this system is discussed. A complete dissertation on the railway engineering is available in *Modern Railway Track* [14] and *Handbook of Railway Vehicle Dynamics* [13].

2.2.1 Railway track System

The typical railway configuration is depicted in Figure 2.3. The main components of a ballasted railway track are the following:

- Rail
- Rail pad
- Fastening system
- Sleeper
- Ballast
- Sub-ballast
- Sub-grade

Rails are characterized, according to the standard EN13674-1, to their mass per unit length $[Kg/m]$, conventionally used as name characterization. The most common types of rail in Europe are UIC60 and UIC54. A rail is characterized by three distinct areas: a rail foot, a rail web, and a rail head. Rails provide a smooth running surface for the train wheels. They carry the vertical and tangential loads coming from the train and distribute them on the sleepers. They also carry electrical signaling for control systems on the line. The higher the mass per unit length of the rail, the higher the global mechanical resistance and inertia of the rail.

Track Gauge is a fundamental parameter expressing the lateral distance between the rails. It is defined in the standard EN13848-1:2003 as the distance between the two points belonging to the rails closest to the other rail and no more than 14mm from the top of the rail vertically on the track coordinate system [15]. The standard gauge in Europe is 1435mm.

Rails are usually mounted with an *inclination angle* with respect to the horizontal plane. The inclination angle is useful in order to tune correctly the equivalent conicity of the wheels. The standard inclination angles are usually 1/20 and 1/40 depending on the geographical area considered.

Rail pads are placed between the rails and the sleepers. They modify the global track stiffness, providing a certain grade of high-frequency isolation. They also permit a higher deflection of the rail and the train load is hence distributed more evenly over the sleepers. They also provide electrical insulation on the rails.

Fasteners are mechanical devices used to constrain the rails on the sleepers reliably. They maintain the track gauge and provide resistance to the vertical, lateral and longitudinal movements of the rails.

Sleepers support the rails and maintain the track gauge and the alignment of the track. The material used for constructing sleepers is commonly concrete, although steel sleepers also exist and timber is sometimes still used. The typical sleeper distance, called *spacing*, is about 600mm.

Ballast, sub-ballast and sub-grade form the bed of the railway track. The ballast layer supports the sleepers embedded in it against vertical and lateral displacements. For instance, the *Proud'homme* limit on sleeper lateral shift depends fundamentally on the maximum lateral force the ballast can impress on the sleeper movement. Ballast is traditionally composed of crushed stones of granite or limestone. Sub-ballast and sub-grade are composed instead of finer stones of lower quality.

In curved tracks, rails are placed with a global inclination angle with respect to the horizontal plane, in order to balance the inertia forces at a standard train velocity. This angle is called super elevation or *Cant* angle. The height difference between the rail heads is called *Cant*.

2.2.2 Track Dynamic Properties

One way for investigating the dynamic properties of a railway track is to perform either a sweep sine excitation force test or a hammer excitation force test. The first test type is used for determining the response of the system up to usually 200Hz. The second test type is instead used for analyzing the response of the railway system at higher frequencies. The dynamic response of the railway track is usually given in the form of a *Receptance FRF*, i.e. the ratio of the track deflection and the force put of the track $[m/N]$ [13], computed at the midspan. The receptance is the inverse of the track stiffness.

Figure 2.4 shows a typical receptance curve in the range 10-1500Hz. Although the receptance of each type of track present several unique aspects, they are usually characterized by some typical resonance peaks. The first one is usually present in the range 50-100Hz and is related to the resonance of the whole track structure on the ballast stiffness. This type of mode is related to the P2 corrugation [4]. Another typical resonance is usually present in the range 200-600Hz and is related to the bouncing of the rail on the rail pad stiffness. The highest resonance peak is associated with the pinned-pinned resonance frequency, which is usually present around 1000Hz. This resonance is usually lightly damped because, since the general eigenmode has

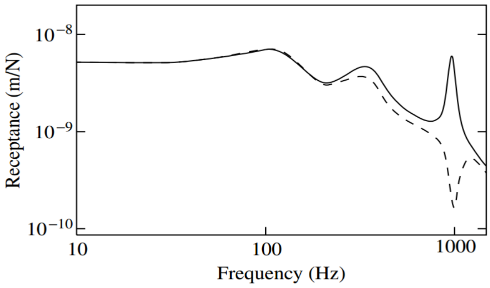

Figure 2.4: Railway track Receptance FRF [9]

nodes near the rail pad, it involves almost only the structural damping of the rail steel [13]. If the receptance is computed at the sleepers, at the pinned-pinned resonance frequency there is an *anti-resonance*, i.e. a minimum in the receptance function, as shown in Figure 2.4. This means that the dynamic track stiffness increases remarkably in this particular conditions.

2.2.3 Vehicle system

The main components of a rail vehicle are depicted in Figure 2.5. A railway vehicle consists of the following main components:

- Car body
- Secondary suspension
- Bogie
- Primary suspension
- Wheelset

Typically every single car of a rail vehicle is supported on two bogies by means of secondary suspension systems. Sometimes two cars can share one bogie. Bogies usually are rigid. Every bogie, in turn, has two wheelsets mounted on it by means of primary suspension systems. Bogies with two suspension stages are called *double suspended*. The primary suspension consists tipically of spring and damper components. Their main task is to reduce the unsprung mass of the system and therefore the total amount of force transferred to the car body. The secondary suspension system usually use either spring and damper or air suspension systems.

A wheelset consists of two wheels and an axle, where the two wheels are rigidly connected by the axle.

Wheels are the most critical part of the system and are generally divided into three categories: solid, tire and resilient types. The most common type is the solid wheel; Tired wheels have a tire shrink-fitted to the wheel that can be replaced when the wear is excessive. Resilient wheels have been designed in order to further reduce the unsprung mass of the vehicle. They have a layer of low elasticity modulus between the wheel and the tire [9].

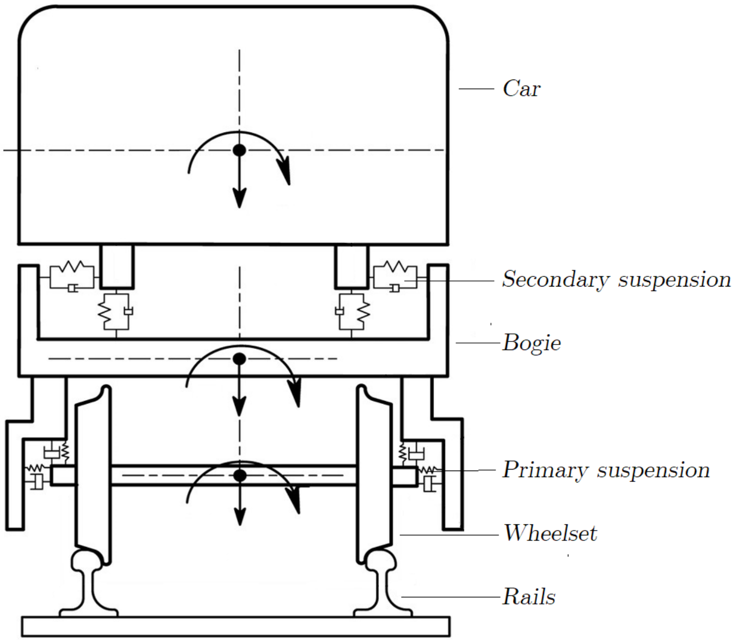

Figure 2.5: Rail vehicle system [16]

2.3 Wheel-rail contact modeling

The determination of the forces acting between wheel and rail and their behavior is the most important question for the study of the dynamic behavior of a railway vehicle. Wheel rail contact forces provide a support action for the vehicle load, a guidance action during the change of direction and during the application of either braking or traction forces [17]. Here a brief introduction on the major contact theories is given.

Generally speaking, the problem can be separated into two steps:

- Normal contact problem
- Tangential contact problem

The solution of the normal contact problem provides the shape and the dimensions of the contact area and the normal contact pressure distribution. The tangential contact problem, provided the solution of the normal contact problem, gives the distribution of the shear contact stress.

The normal contact problem and the tangential contact problem are generally speaking coupled problems. Without any assumptions, the problem is of considerable complexity. However, several common assumptions are usually adopted in order to get a simple solution of the problem.

2.3.1 Assumptions

The most common assumptions employed in the main wheel-rail contact models are briefly listed.

- *Elastic assumption*: The deformation of the bodies in contact is considered as purely elastic;
- *Non-conformal contact*: The bodies are dissimilar enough that, under zero load, they only touch at a point or a line. A conformal contact would involve instead bodies that touch at multiple points before any deformation takes place. Under this assumption, the dimensions of the contact area are small compared to the local dimensions of the bodies in contact, i.e. their local curvature radii [18];
- The elastic characteristics of the bodies in contact (E, ν) are similar;
- *Quasi-identical assumption*: The bodies in contact are assumed to be quasi-identical if all the previous assumptions listed are considered in the modeling.

The *Elastic-half space assumption* considers the elastic and the non-conformal contact assumptions. If the Quasi-identical assumption holds, the normal contact problem is decoupled from the tangential one.

2.3.2 Main contact theories

Normal problem

Hertz theory [19] provides the analytical solution to the normal contact problem. Hertz demonstrates that when two elastic bodies are pressed together under the following conditions:

1. Elastic half space assumption
2. Constant curvature inside the contact patch

then:

- The contact area is an ellipse
- The contact area is considered *flat*
- The contact pressure is a semi-ellipsoid

Considering x and y the longitudinal and lateral principal directions, and considering the center of the elliptic contact area as the origin, the distribution of normal contact pressure is obtained as:

$$p(x, y) = p_0 \sqrt{1 - \left(\frac{x}{a}\right)^2 - \left(\frac{y}{b}\right)^2} \tag{2.3.1}$$

where a and b are the major and minor axes of the elliptic contact area respectively, their values depending on the material properties of the contacting solids, the radii of curvature and the normal contact force applied. The term p_0 is the maximum contact pressure at the center of the contact patch, i.e.:

$$p_0 = \frac{3}{2} \frac{N}{\pi a b} \tag{2.3.2}$$

The solution of the normal contact problem is needed for solving subsequently the tangential contact problem. Generally, the normal contact problem is solved by using Hertz's theory.

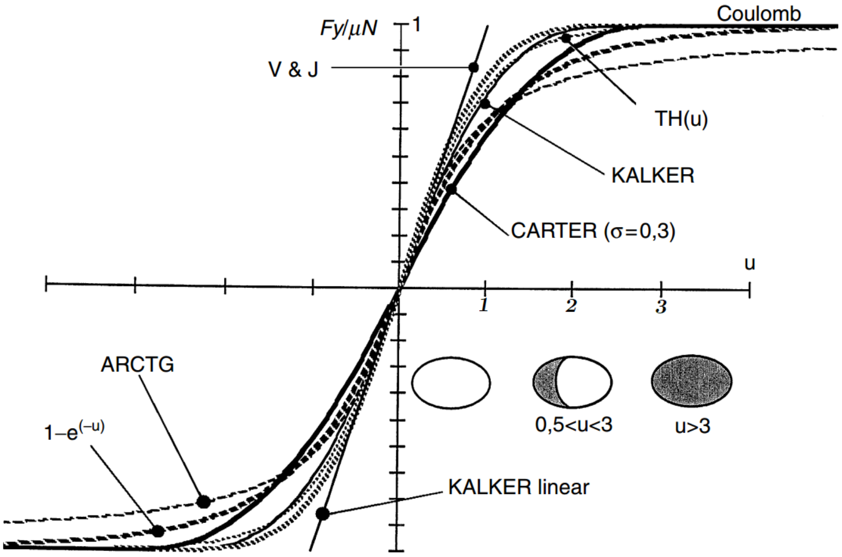

Figure 2.6: Rolling contact and Coulomb's models for sliding friction [9]

Tangential problem

The resolution of the tangential problem has been the question that has focused the attention of researchers, leading to defining several theories. Tangential forces arise due to the relative motion between wheel and rail, usually referring to the latter as pseudo-sliding, micro-creepage or simply creepage [17]. With no relative motion between wheel and rail, no tangential contact forces can be present.

The simplest tangential contact model comes from *Carter's theory*. From the first experiments performed by Carter in the 1930s, evidences showed that by increasing the traction force applied to the leading wheelsets, instead of having a sudden transition between a condition of full adhesion to a condition of full sliding when the traction force reaches the maximum allowable, i.e. μN, there is a gradual transition between the two conditions. The contact area is considered to be divided into a sliding area (on the trailing side) and an adhesion area (on the leading side), whose proportions vary with respect to the applied tangential force applied. The higher the traction force, the higher the creepage, larger the sliding area. Considering a monodimensional model referring only to the longitudinal direction, the relative motion condition can be expressed defining the *longitudinal kinematic creepage* as:

$$\xi_x = \frac{\omega r_0 - V_0}{\omega r_0} \tag{2.3.3}$$

where V_0 is the longitudinal velocity of the vehicle, ω is the angular velocity of the wheel and r_0 is the rolling radius. $\xi_x = 1$ corresponds to a complete slip condition in which the wheel rotates with no longitudinal velocity. Figure 2.6 shows the typical rolling friction tangential force model's behavior as a function of the longitudinal kinematic creepage, defined by using different models, in contrast to the classical sliding friction Coulomb's model.

For small values of creepage, the tangential contact force is linearly proportional to the creepage itself, and the slip is governed by the elastic deformation of the bodies.

By increasing the creepage, the tangential contact force increases non-linearly until it reaches the maximum allowable value determined by the Coulomb's law, i.e.: $\mu_d N$.

In 1964 *Vermeulen & Johnson* developed a more refined tangential contact theory that took into account both longitudinal and transversal creepages. The contact area is considered elliptic as well as the adhesion area. The latter is tangent to the contact area ellipse at a single point corresponding to the leading edge. These assumptions lead to relevant errors due to the missing transition between the adhesion and the sliding areas.

Kalker's theory is the basis of the modern contact theories. In this case, the contact area is considered elliptical with the simultaneous presence of longitudinal, lateral and spin creepage. The *Kalker's linear theory* gives a method to calculate the contact forces in the linear portion of the force-creepage curve.

The *Kalker's non-linear theory* gives the distribution of the tangential forces at high creepages values and therefore in the non-linear part of the curve. The maximum tangential stress at each contact point inside the contact area is:

$$\tau(x,y) \leq \mu p(x,y) \tag{2.3.4}$$

Introducing the local slip $s_\tau(x,y)$, achievable through the kinematic creepages, it is possible to define the local tangential stress value:

$$\begin{cases} \tau(x,y) = -\mu p(x,y)\frac{s_\tau(x,y)}{|s_\tau(x,y)|} & \text{if } |s_\tau(x,y)| \neq 0 \\ \tau(x,y) = 0 & \text{if } |s_\tau(x,y)| = 0 \end{cases} \tag{2.3.5}$$

The most known algorithms for the computation of the tangential stress are CONTACT (commercial) and FASTSIM (free license), implemented by Kalker himself.

A complete dissertation on the normal and tangential contact theories is available in [20], [17], [13].

2.3.3 ABAQUS FE Contact Modeling

A complete dissertation about contact modeling in ABAQUS is available in [21].

Definition of contact interactions in ABAQUS is generally made up of several stages. A first fundamental stage is the *Contact interaction definition*, where the definition of the algorithms used to define the contact domains in the model is performed. The second procedure is the definition of *Contact properties*, i.e. the definition of the mathematical laws that govern the specific interaction between the contacting bodies. The third and last stage is the *Contact formulation*, where the algorithms that govern several aspects of the implementation, i.e. the contact discretization, the tracking approach and assignment of the surface role (master/slave) in the contact interaction, are selected. In the following chapter, the general characteristics of these stages are briefly described.

Contact interaction definition

In Abaqus/Standard, the approaches available for defining the contact interaction are the following:

- General contact;
- Contact pairs;
- Contact elements;

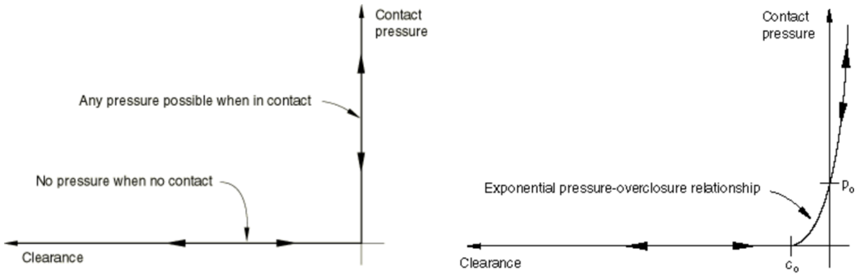
Contact pressure
Any pressure possible when in contact
No pressure when no contact
Clearance
Contact pressure
Exponential pressure-overclosure relationship
p₀
Clearance
c₀

Figure 2.7: *Hard* (a) and *Softened-exponential* (b) pressure-overclosure relationships [21]

General contact and Contact pairs are surface-based approaches, i.e. the contact interaction is defined by defining the surface of the bodies that could potentially be in contact. The surface selection can be performed by specifying *surface pairings* or *self-contact surfaces*. The first type of selection involves the definition of two surfaces (a pair) that interact only with each other, while the second type involves a generalized surface (it could be defined by multiple surfaces) that interact only with itself. Typically, general contact interactions are defined by using self-contact surfaces in order to get a flexible definition of contact. Instead, contact pairs use surface pairings as the surface selection method. Contact elements can be used when contact cannot be simulated with the common surface-based approach. They are seldom used.

Contact properties

In an ABAQUS contact simulation, the interaction between contacting bodies is defined by assigning a contact property model to a contact interaction. By default, the only normal contact mechanical interaction is present, defining a penetration constraint between the bodies. In addition, property models can include for several constitutive properties.

Model for the normal contact interaction The normal contact interaction is typically described in terms of a *contact pressure-overclosure relationship*, considering that *overclosure* is the relative penetration of the contacting surfaces. The default relation is referred to as the *Hard contact*, i.e. the surfaces transmit no contact pressure unless a contact between them is initialized. No overclosure is permitted. *Softened* relationships are present in ABAQUS. Figure 2.7 shows the difference between a *Hard* and a *Softened* pressure-overclosure relationship. The most common relationship is the Hard contact. The pressure-overclosure relationship may or may not be strictly enforced depending on the so-called *Constraint Enforcement Methods*, i.e. the type of algorithm used to solve numerically the contact analysis. Three constraint enforcement methods are available:

- *Direct method*: Direct application of the pressure-overclosure relationship. It is the easiest implementation but leads to overconstraint issues.
- *Penalty method*: Stiff approximation of the Hard contact. The contact force is considered proportional to the penetration distance between the surfaces. The relationship can be therefore expressed, at a node i as:

$$\underline{f_i} = -\delta_i K_i \underline{n_i} \tag{2.3.6}$$

where K_i is the contact stiffness, δ_i the overclosure between the contacting surfaces at that particular position and n_i the vector normal to the surface. Contact stiffness can vary either linearly or non-linearly with respect to the overclosure.

- *Augmented Lagrange method*: Based on a linear penalty method used within an iteration procedure that minimizes the effective overclosure between the surfaces. It is therefore a more accurate method with respect to the penalty method alone, yet more time-consuming due to the higher number of iterations.

Model for the tangential contact interaction :

The tangential contact interaction, also known as the friction model between the contacting bodies, can be described in ABAQUS in different ways. By default, the interaction is *frictionless*. This contact model is seldom used since it doesn't lead to a definition of tangential contact forces.

The tangential contact interaction is modeled in order to get a relation between the frictional stress and the contact pressure between the contacting bodies. At first, the maximum allowable frictional stress is needed; the model known as the classic *Coulomb friction model* is used. The Coulomb friction model defines a maximum shear stress $\tau_{max} = \mu p$ at which the contacting surfaces transition from a sticking state to a sliding state. The friction of coefficient μ is by default isotropic.

There are two main ways to define the complete friction model in ABAQUS.

- *μ defined as a function of the slip rate and contact pressure $\mu = \mu(\xi, p)$*: This is what is also called *Penalty method*, because of the enforcement method used. The friction coefficient can be defined in general as a function of the equivalent slip rate and the contact pressure. One can set a further dependence on the temperature on the contact and on the generalized field variables.

- *Definition of a static and a dynamic friction coefficient*: The friction coefficient can be defined in two extreme conditions, i.e. a complete sticking condition and a complete sliding condition, leading to the definition of a static and a dynamic friction coefficient. The latter is smaller than the former. The friction coefficient decays exponentially from the static value to the dynamic value according to:

  $$\mu = \mu_d + (\mu_s - \mu_d)e^{-\alpha\xi}$$

  where α is a decay coefficient.

The tangential contact can be enforced by using *Lagrange multipliers*, as well as in the case of normal contact.

Contact formulation

A contact formulation involves a series of choices on the contact numerical implementation. There are three main choices to be made, i.e.:

- How the contact surfaces are discretized during the integration (*contact discretization*). Contact discretization is needed in order to apply the conditional constraints that simulate the contact interaction. There are two types of contact discretization:

  - *Node-to-surface*: Traditional discretization method. Each slave node interacts with a point of projection on the master surface. The contact involves therefore for each slave node a group of master nodes from which values are interpolated to the projection point. Penetration of the master surface on the slave surface can occur.
  - *Surface-to-surface*: Discretization method that considers the shape of both slave and master surfaces. The contact condition is distributed over regions near the slave nodes in an average sense, leading to a smoothing effect of the contact conditions over the region.

  Surface-to-surface generally gives more accurate results than the node-to-surface method and no large penetration of the master surface on the slave surface occurs.

- How the relative motion between the contacting surfaces is mathematically defined (*Tracking approach*). In Abaqus/Standard, there are two different tracking approaches:
  - *Finite sliding*: Most general and allows for any arbitrary motion of the surfaces.
  - *Small sliding*: Although two bodies can undergo large motions, there will be little *sliding* on one surface along the other.
- Assignment of *master* and *slave* roles to the contacting surfaces.

2.4 Wear

Wear is the gradual removal of material obtained during the contact interaction of surfaces in relative motion. Wear phenomena are hence strictly associated with frictional processes between the surfaces. Many wear mechanisms have been identified; the most common wear types are the following:

- *Adhesive Wear*: Adhesive wear is produced by the formation and subsequent shearing of welded joints between two contacting surfaces. This type of wear is commonly found during contact between bodies made of the same material;
- *Abrasive Wear*: Abrasive wear occurs when a hard rough surface slides across a softer surface;
- *Surface Fatigue Wear*: Wear on solid surfaces due to propagation of fatigue fractures;
- *Corrosive Wear*;

Wear is commonly modeled using the Archard's simplified wear theory first developed in 1953 [22]. The model considers adhesive wear and makes the assumption that the volume of removed material is proportional to the dissipated sliding energy, which in turn is the work done by the frictional forces. Therefore, Archard's wear is formed only in presence of relative creepage. The volume of removed material due to wear is

$$V = K\frac{N}{H}\xi \tag{2.4.1}$$

where N is the normal load, H the hardness of the softer of the two contacting bodies, ξ is the sliding distance and K the *wear coefficient*, which is often used to compare the material wear resistance and estimated experimentally. Typical values of K range between 10^{-8} for a lubricated incompatible materials interaction and 10^{-3} for an unlubricated interaction with similar materials.

Equation 2.4.1 shows the relationship between normal contact force and wear material volume removed during the contact interaction. If the normal contact force varies with time due to contact non-steadiness, the volume of material removed by the wear process will vary as well.

Considering the rail-wheel interaction, vibrations of the rail due to a wavelength-fixing mechanism such as self-excited vibrations generated by saturated creep forces can influence the contact condition, leading to time varying contact forces, a time-varying wear rate and hence a longitudinal corrugation of the rail head. An interesting study on the correlation between self-excited vibrations and fluctuation of the normal contact forces has been performed by Chen et al. through a comparison of a self-excited vibrations analysis and a transient-dynamic analysis [10].

2.5 Complex Eigenvalue Analysis

The complex eigenvalue analysis, also known as C.E. analysis, has been widely used by researchers. It has been mainly used as a tool for predicting unstable frequencies in friction-induced vibration problems. This method deals with the computation of system eigenvalues and their corresponding mode shapes which in general are complex-valued functions, and the deployment of the eigenvalues real part as a parameter correlated to the particular mode shape stability. In general, the system might experience instability because friction forces cause the stiffness matrix to be asymmetric [23]. ABAQUS versions 6.4 and above provide the implementation of the complex eigenvalue analysis for the stability prediction of friction-induced vibration FE models. For more pieces of information about the ABAQUS analysis procedure, see Chapter 3.5.1.

One of the major applications of the CEA is on the prediction of brake squeal instabilities.

In 2006, AbuBakar and his group [24, 25] has used the CEA together with a transient dynamic analysis for predicting break squeal frequencies, and the effect of temperature-dependent friction of the break stability. In 2007, Liu and his group [26] has performed a parametric analysis of brake squeal by using the same method. In 2009, Nouby et al. [23] has for the first time integrated the CE analysis with a design of experiment analysis in order to perform a parametric analysis of disc brake squeal by using statistical regression techniques.

More recently, the CEA has been used in order to study both rail corrugation and wheel-rail squeal under the point of view of saturated creep forces self-excited vibrations [27, 10, 28].

In their works, Chen and his group has used the CE analysis, together with a transient dynamic analysis, for the prediction of rail corrugation induced by self-excited vibrations. In 2016, Goo et al. [29] has used the complex eigenvalue analysis for the prediction of wheel-rail squeal during tight train curve negotiation.

2.5.1 Complex eigenvalue extraction

Generally speaking, the equations of motion of a discrete (n degrees of freedom) mechanical system are:

$$[M]\underline{\ddot{x}} + [C]\underline{\dot{x}} + [K]\underline{x} = \underline{q} \tag{2.5.1}$$

where $[M]$, $[C]$ and $[K]$ are respectively the mass, damping and structural stiffness matrices of the system (nxn), while $\underline{q}$ is the vector of the generalized external forces acting on the system. The structural matrices of the system are generally positive definite. In the case of a structural/mechanical FE model, the vector $\underline{x}$ represents all the degrees of freedom of the mesh nodes.

In the case of the wheel-rail contact problem, under the self-excited vibrations wavelength-fixing mechanism theory, the friction forces field is assumed to be the main cause of generated vibration [29].

The vector of external forces $\underline{q}$, consisting only on the friction forces, can be defined as a function of the displacement of the two contacting bodies on the contact patch and on its localized contact stiffness:

$$\underline{q} = \mu[K_f]\underline{x} \tag{2.5.2}$$

where $[K_f]$ is the friction stiffness matrix, generally *not* positive definite, and μ the friction coefficient function on the contact patch.

The governing equations can hence be rewritten as:

$$[M]\underline{\ddot{x}} + [C]\underline{\dot{x}} + [[K] - \mu[K_f]]\underline{x} = \underline{0} \tag{2.5.3}$$

where $[[K] - \mu[K_f]]$ is in turn not symmetric. Since the global stiffness matrix is not symmetric, the system might manifest flutter instability of various modes of the system.

The characteristic equations of the system can be expressed as:

$$(\lambda^2[M] + \lambda[C] + [[K] - \mu[K_f]])\underline{\phi} = \underline{0} \tag{2.5.4}$$

where λ are the system eigenvalues and $\underline{\phi}$ the eigenvectors of the system. In general, Equation 2.5.4 gives complex eigenvalues. It is not trivial solving an eigenvalue problem with a not symmetrical stiffness matrix. Therefore, in order to get a simpler solution of the problem solver softwares usually use approximation methods. The most common one is the so-called *subspace projection method*.

2.5.2 Subspace projection method

In the subspace projection method, the original eigensystem is projected onto a subspace spanned by the eigenvectors of the undamped, symmetric system [21]. In absence of the damping and friction terms, Equation 2.5.4 reduces to a symmetric problem:

$$(\lambda_r{}^2[M] + [K])\underline{\phi_r} = \underline{0} \tag{2.5.5a}$$

$$det(\lambda_r{}^2[M] + [K]) = \underline{0} \tag{2.5.5b}$$

where $\underline{\phi_r}$ are the eigenvectors of the reduced system. Equation 2.5.5b can be easily solved by means of well-implemented iteration methods for the extraction of eigenvalues and the corresponding eigenvectors of a *symmetric* generalized eigenproblem, e.g. Lanczos or AMS methods. Further details about these methods are present in [21]. In general, the eigenvalue extraction is stopped before a complete extraction at a user-defined number of eigenvalues m, commonly in the order of 10^2 - 10^3.

With the reduced solution, all the structural matrices of the original system can be projected into the reduced eigenvector subspace.

$$[M^*] = [\Phi_r]^T[M][\Phi_r] = \{\underline{\phi_{r1}}, \underline{\phi_{r2}}, \dots, \underline{\phi_{rm}}\}^T[M]\{\underline{\phi_{r1}}, \underline{\phi_{r2}}, \dots, \underline{\phi_{rm}}\} \tag{2.5.6a}$$

$$[C^*] = [\Phi_r]^T[C][\Phi_r] = \{\underline{\phi_{r1}}, \underline{\phi_{r2}}, \dots, \underline{\phi_{rm}}\}^T[C]\{\underline{\phi_{r1}}, \underline{\phi_{r2}}, \dots, \underline{\phi_{rm}}\} \tag{2.5.6b}$$

$$[K^*] = [\Phi_r]^T[K][\Phi_r] = \{\underline{\phi_{r1}}, \underline{\phi_{r2}}, \dots, \underline{\phi_{rm}}\}^T[K]\{\underline{\phi_{r1}}, \underline{\phi_{r2}}, \dots, \underline{\phi_{rm}}\} \tag{2.5.6c}$$

With the projected structural matrices of the system, the differential equations of motion in the modal subspace can be written as follows:

$$[M^*]\underline{\ddot{y}} + [C^*]\underline{\dot{y}} + [K^*]\underline{y} = \underline{0} \tag{2.5.7}$$

Where $\underline{y}$ is the vector of the modal coordinates, defined as:

$$\underline{x} = [\Phi_r]\underline{y} \tag{2.5.8}$$

The projected characteristic equations thus become:

$$({\lambda_p}^2[M^*] + \lambda_p[C^*] + [[K^*]])\underline{\phi_p} = \underline{0} \tag{2.5.9}$$

With respect to the very large number of equations to be solved in Eq.2.5.4, equal to the number of degrees of freedom of the FE model, the number of equations in Eq.2.5.9 is equal to the number of natural eigenmodes used for the subspace projection, thus leading to a way faster numerical integration. This equation is then solved using the standard QZ method for generalized non symmetric eigenproblems.

Eq.2.5.7 is generally rewritten by using the 2n-dimensional state variable vector approach, obtaining:

$$\underline{\dot{z}} = [A]\underline{z} \tag{2.5.10}$$

where:

$$\underline{z} = \begin{bmatrix} \dot{y} \\ y \end{bmatrix} \tag{2.5.11}$$

$$[A] = \begin{bmatrix} [M^*] & \mathbf{0} \\ \mathbf{0} & [M^*] \end{bmatrix}^{-1} \begin{bmatrix} -[C^*] & -[K]^* \\ [M^*] & \mathbf{0} \end{bmatrix} \tag{2.5.12}$$

By solving the characteristic equations:

$$det(\lambda_p[I] - [A]) = \underline{0} \tag{2.5.13}$$

it is possible to obtain the eigenvalues and eigenvectors of the asymmetrical damped system projected in the subspace.

The QZ numerical method can be applied, by decomposing $[I]$ and $[A]$ into their *Shur* forms such that:

- if $[A]$ and $[B]$ are real

$$[A] = [Q][S][Z]^T \tag{2.5.14a}$$

$$[I] = [Q][T][Z]^T \tag{2.5.14b}$$

- if $[A]$ and $[B]$ are complex

$$[A] = [Q][S][Z]^H \tag{2.5.15a}$$

$$[I] = [Q][T][Z]^H \tag{2.5.15b}$$

where $[Q]$ and $[Z]$ are unitary and $[S]$ and $[T]$ are upper triangular.

The eigenvalues $\underline{\lambda_p}$ that solve the generalized eigenvalue problem in eq 2.5.13 is an unknown nonzero vector and :

$$\lambda_{p_i} = \frac{[S]_{ii}}{[T]_{ii}} \tag{2.5.16}$$

Finally, the eigenvectors of the original system can be approximated by projecting the obtained eigenvectors in the original n d.o.f. space:

$$\underline{\phi} \simeq \{\underline{\phi_{r1}}, \underline{\phi_{r2}}, \ldots, \underline{\phi_{rm}}\}\underline{\phi_p} \tag{2.5.17}$$

Usually, also in the case of the final complex eigenvalues and eigenvectors the extraction arrests at a user-defined number of eigenvalues.

The complex eigenvalue λ_k can be expressed by means of its real and imaginary components $\lambda_k = \alpha_k \pm i\omega_k$. The general solution of the system can be obtained by superimposing the single eigenmodes:

$$x(t) = \sum_{k=1}^{n} \phi_k e^{\lambda_k t} = \sum_{k=1}^{n} \phi_k e^{(\alpha_k \pm i\omega_k)t} \tag{2.5.18}$$

The real part of the eigenvalue is the basis of the judgment of system stability. It can be found that when the real part of an eigenvalue is larger than zero, the nodal displacement $x(t)$ will increase with time, which means that the vibration of the system is growing and the system will become unstable [28].

A common parameter used to measure the propensity of self-excited vibration occurrence is the definition of an *effective damping ratio* for every single eigenmode of the system.

$$\delta_k = -2\frac{Re(\lambda_k)}{Im(\lambda_k)} \tag{2.5.19}$$

If the damping ratio is negative, the eigenmode considered is supposed to be unstable and has a tendency to induce self-excited vibrations.

Chapter 3

Method of Analysis

The overall analysis methodology adopted in this thesis combines a first stage of *Multi-Body* simulations in order to define correctly the boundary conditions of the *Finite-Elements* model, and FE analyses conducted by means of the general purpose FE software *ABAQUS*. In order to perform the analysis, the modeling process lies on several assumptions. Only one car body is considered in the dynamic analysis, as well as only the leading wheelset of the leading bogie is considered in the main FE model, since according to [8] the characteristic corrugation type in curve, i.e. rutting, occurs due to roll-slip instabilities of the leading wheelset due to a saturation of the tangential creep forces. Therefore, no interaction effects of the remaining wheelsets on the instability of the coupled vehicle-track system are considered. Moreover, since the nature of the analysis is a perturbation analysis around the neighborough of a steady-state dynamic condition, no dynamic effects, as well as non-linear effects on the instability of the system are taken into account.

3.1 FE Analysis

The overall analysis of this research is conducted by using the general purpose finite element program ABAQUS, specifically the 6.14 version, and by following the instruction of the related *Abaqus 6.14 Documentation*. The following sections provide a brief summary of ABAQUS program and its structure.

3.1.1 ABAQUS structure

ABAQUS is a set of finite element programs developed by Hibbit, Karlsson & Sorensen, Inc. in 1978 and maintained by SIMULIA Corp. ABAQUS is a general-purpose analyzer and can solve a wide range of engineering problems. ABAQUS is a package consisting of three main products: *ABAQUS/CAE*, *ABAQUS/Standard* and *ABAQUS/Explicit*. ABAQUS/CAE provides a graphical environment for the modeling process (*pre-processing*) and for the results manipulation (*post-processing*).

ABAQUS/Standard is a general-purpose Finite-Element analyzer that employs an implicit integration procedure for solving linear, nonlinear, static & dynamic analysis.

In this research, ABAQUS/CAE and ABAQUS/Standard are employed.

Figure 3.1 depicts the three fundamental stages for an ABAQUS simulation: pre-processing, simulation and post-processing.

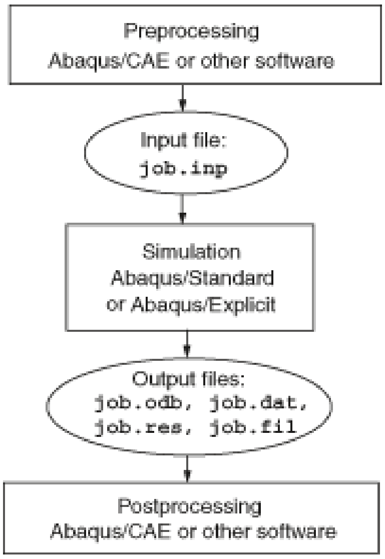
Preprocessing
Abaqus/CAE or other software
Input file:
job.inp
Simulation
Abaqus/Standard
or Abaqus/Explicit
Output files:
job.odb, job.dat,
job.res, job.fil
Postprocessing
Abaqus/CAE or other software

Figure 3.1: ABAQUS stages for a full simulation [21]

A complete analytical model in ABAQUS includes the definition of 10 modules: *Part*, *Property*, *Assembly*, *Step*, *Interaction*, *Load*, *Mesh*, *Job*, *Visualization*, *Sketch*.

In order to get a complete analysis model, it is necessary to define most of these modules:

- Define the model geometry through a set of parts (Part module, Mesh module, Sketch module);
- Create material sections & assign them to the parts (Property module);
- Assemble the parts in order to get the global structure geometry (Assembly module);
- Create the analysis steps (Step module);
- Create model interactions between parts and define loads and boundary conditions along the analysis (Interaction module, Load module);
- Mesh the model (Mesh module);
- Create jobs and submit them for analysis (Job module);
- Analysis of the results (Visualization module);

3.2 Dynamics

The steady-state dynamic condition in a curved track of the system is necessary in order to set correctly the FE model for the CE analysis. The necessary input data coming from the dynamics are essentially the suspension forces acting on the wheelset bearings. Therefore, in order to have a reference steady-state curved condition, it is possible either to consider an approximated state by using balance equations or to

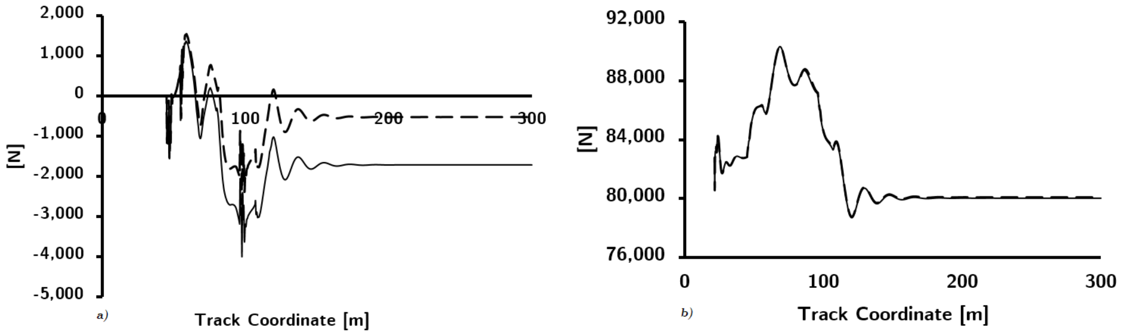

Figure 3.2: High leading wheelset suspension forces: a) *Lateral forces* b) *Vertical forces*; (—) Gauge: 1435 mm, (- - -) Gauge: 1455 mm

perform a preliminar *multibody* simulation on a reference model. Generally, the latter strategy is more time-consuming but more reliable than the former one. In this thesis, the steady-state condition was obtained from MBS simulations.

The reference velocity considered is 40 Km/h.

3.2.1 Reference track

The corrugation design of experiments sensitivity analysis considers track Gauge as one of the parameters investigated (see Chapter 3.6). Moreover, track Gauge is the only parameter of the analysis that could affect remarkably the MBS results. For this reason, two different MBS models are used: the first one with a standard Gauge equal to *1435* mm and the second one with a widened Gauge equal to *1455* mm.

The total length of the modeled MBS track is 300m. The track is divided into three distinct sections: a *straight* section, a *transition* section, and a *curved* section. The first section is 24 meters long. The transition section is 51 meters long. The transition curve is used in order to reduce the magnitude of the lateral accelerations the car would have experienced if the switch had been directly from the straight line section to the curved one. The curved section is 225 meters long. The radius of curvature of the curved track is set to 300m. It is worth to mention that it is not necessary to run the MBS simulation on the whole length of the model, since the curved steady-state condition of the system occurs before the completion of the whole simulation.

Cant is set in order to have a super elevation of the high rail with respect to the low rail equal to 100mm, while the inclination angle of the rails is equivalent to 1/20.

3.2.2 Reference train

In the MBS model considered, the train has only one car due to computational time issues. The car lies on two bogies, a leading on the front and a trailing on the rear. Each bogie has a leading wheelset and a trailing one. The wheelsets are not motorized. The weight of the car and of a single bogie are 47.5 Ton and 10 Ton, respectively.

3.2.3 MBS Output

As a reference, the vertical forces are positive if pointing upwards while the lateral forces are positive if pointing towards the field side. The positive yaw angle are

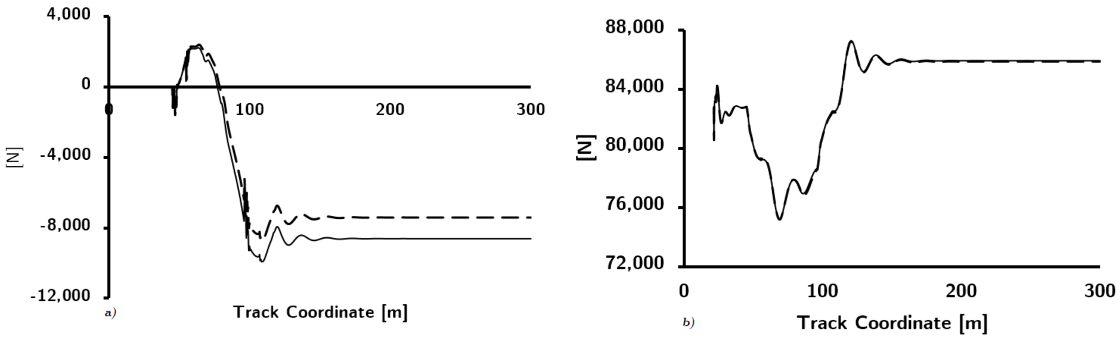

Figure 3.3: Low leading wheelset suspension forces: a) *Lateral forces* b) *Vertical forces*; (—–) Gauge: 1435 mm, (- - -) Gauge: 1455 mm

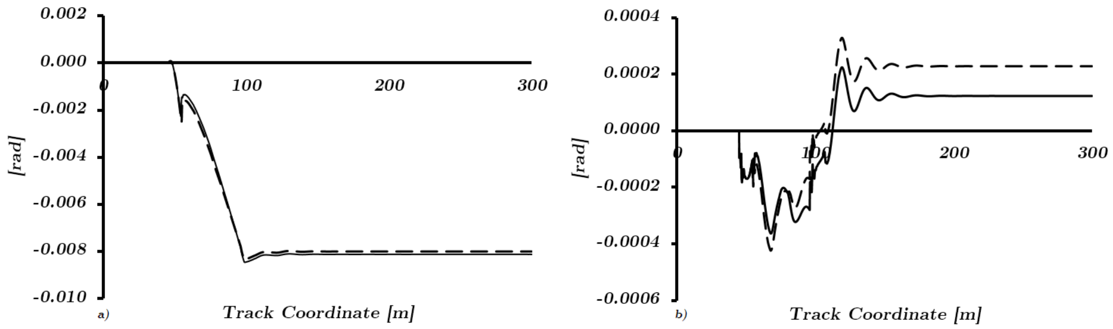

Figure 3.4: a) *Leading wheelset Yaw angle* b) *Leading wheelset Roll angle*; (—–) Gauge: 1435 mm, (- - -) Gauge: 1455 mm

Table 3.1: MBS steady state results

		Gauge: 1435 mm	Gauge: 1455 mm
$F_{high,v}$	[N]	-80000	-80000
$F_{low,v}$	[N]	-85900	-85900
$F_{high,l}$	[N]	1710	523
$F_{low,l}$	[N]	8610	7400
Yaw, ψ	[rad]	-0.00812	-0.0080
$Roll, \rho$	[rad]	0.000123	0.000228

positive in clockwise direction.

Figures 3.2 and 3.3 depict the lateral and vertical suspension forces of the leading wheelset respectively on the high side bearing (outside curve side) and on the low side bearing (inside curve side). Figure 3.4 depicts the leading wheelset *yaw* and *roll* angles. The MBS results are given both for the case of a standard gauge and for the case of a widened gauge. As one can see, during the transition section and part of the curved section, hence for a track coordinate between 50m and 150m ca., the force values, as well as the yaw angle value, change remarkably due to unsteadiness. In the second part of the curve section, the values reach a steady state condition.

Table 3.1 depicts the steady state MBS results. While the vertical suspension forces are not affected by the track gauge difference, the lateral suspension forces decrease in the case of a wider gauge. The yaw angle magnitude is bigger in the case of a smaller track gauge, while the roll angle magnitude is smaller to a small degree.

3.3 Modeling Process

3.3.1 Geometries

The analysis considers standard geometries and wheel profiles. In the next sections, the basic model geometries are discussed.

Rails

The most common rail geometries are essentially the UIC60 and UIC54. However, in the commercial rail lines, the UIC60 is by far the most common one. Hence, a standard UIC60 is considered as transversal rail section in this analysis. In Figure 3.5 the standard scheme of a UIC60 rail is depicted.

Wheel

In the analysis, two different wheel profiles are used. Specifically, a typical European wheel profile and a Chinese wheel profile used in Metro lines.

A complete transversal specific European wheel geometry couldn't be found easily. Nevertheless, the most common type of wheels used is a solid S-shaped wheel. Therefore, in order to get the necessary geometries for the analysis, a standard profile from the Italian railway administration is used [31]. The wheels have a rolling diameter of 920 mm, an axle diameter of 180 mm and a *new* wheel profile. In Figure 3.6 the scheme of the transversal section of the European wheel is depicted.

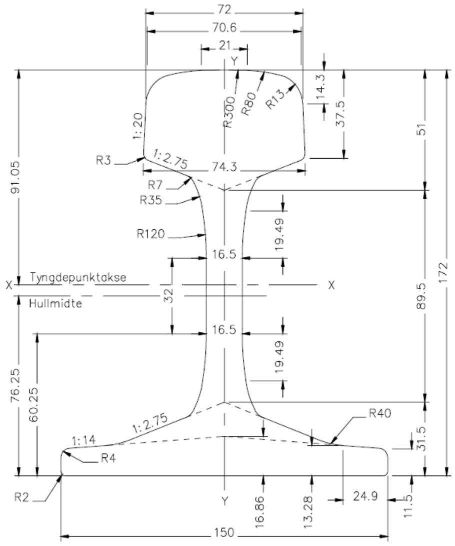
72
70.6
21
Y
R300
R80
R13
14.3
37.5
51
1:20
R3
1:2.75
74.3
R7
R35
R120
16.5
19.49
91.05
X
Tyngdepunktakse
Hullmidte
32
X
89.5
172
16.5
19.49
76.25
60.25
1:2.75
R40
1:14
R4
31.5
R2
Y
16.86
13.28
24.9
11.5
150

Figure 3.5: UIC60 Standard rail profile [30]

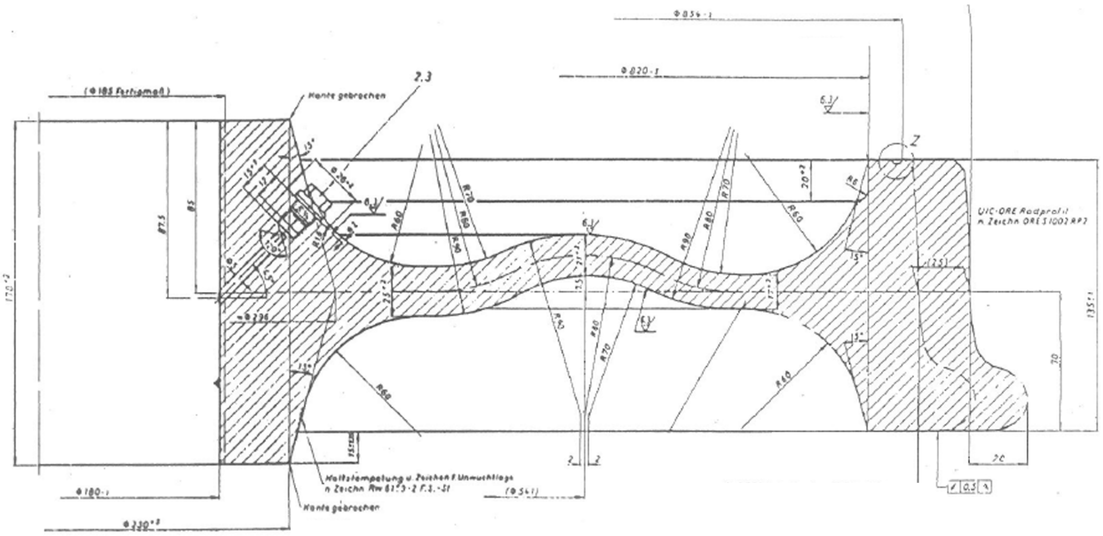
(Φ185 Fertigmaß)
Kante gebrochen
2.3
Φ820-1
Φ854-1
6.3
Z
20+2
R6
R60
R70
R80
R90
R60
6.3
UIC-ORE Radprofil
n. Zeichn. ORE S1002 RP7
87.5
85
170+2
≈Φ296
25+2
15°
13°
(25)
135±1
70
R60
R40
R80
R70
R60
2
2
Kaltstempelung u. Zeichen f. Unwuchtlage
n. Zeichn. Rw 61.3-2 F.3.-31
(Φ541)
Kante gebrochen
Φ180-1
Φ230+3
70
0.5

Figure 3.6: Transversal S-shaped European wheel profile [31]

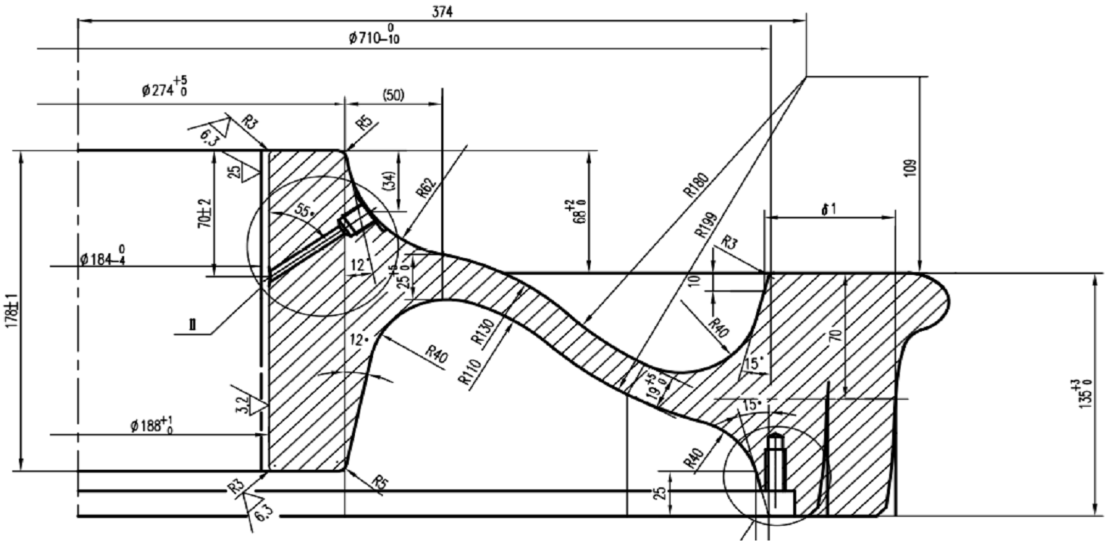
374
$\phi 710^{0}_{-10}$
$\phi 274^{+5}_{0}$
(50)
R3
6.3
R5
25
70±2
(34)
R62
55°
12°
$\phi 184^{0}_{-4}$
178±1
II
68^{+2}_{0}
R180
R199
R3
ø1
109
10
R40
70
15°
12°
R40
R130
R110
19^{+5}_{0}
3.2
$\phi 188^{+1}_{0}$
15°
R40
25
R3
R5
6.3
135^{+3}_{0}

Figure 3.7: Transversal SFMZ06M1 Chinese wheel profile [10]

The Chinese wheel profile, labeled *SFMZ06M1*, is the same used by Chen et al. [10] in their study on severe *rutting* corrugation of Metro lines in China. In the literature, researchers think this corrugation case was caused by the very low vertical support stiffness of the Cologne-egg type fastener used in the Chinese metro lines. The wheels have a rolling diameter of 840 mm, an axle diameter of 180 mm and a *new* wheel profile. In Figure 3.7 the scheme of the transversal section of the Chinese wheel is depicted.

Wheel profile

The wheel profile used is a new standard ORE S1002. According to the European standard EN 13715 [33], the fundamental dimensions defining the contact profile depend on the flange height and thickness. For a wheel diameter of 920mm, the two dimensions are respectively 28 mm and 32.5 mm.

In Figure 3.9 is depicted the contact profile scheme for the previously defined case.

Sleeper

According to the standard EN 13674-1, concrete sleepers are delivered in two versions regarding rail profiles:

- 60E1 sleepers (JBV60): Concrete mono block sleeper for rail profile 60E1;
- 54E3 sleepers (JBV54): Concrete mono block sleeper for rail profile 54E3 and 49E1;

The sleeper geometry used is a standard JBV60, which is consistent with the UIC60 rail profile. In Figure 3.8 are depicted the sections of the standard sleeper used.

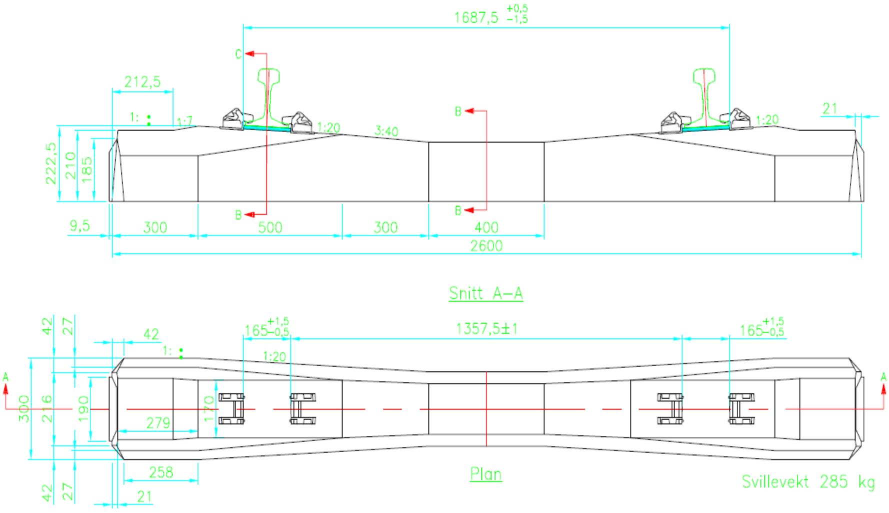
1687,5 +0,5 −1,5
212,5
1:
1:7
C
1:20
3:40
B
1:20
21
222,5
210
185
B
B
9,5
300
500
300
400
2600
Snitt A–A
42
27
42
1:
165 +1,5 −0,5
1:20
1357,5±1
165 +1,5 −0,5
A
300
216
190
170
279
A
258
21
42
27
Plan
Svillevekt 285 kg

Figure 3.8: JBV60 Sleeper profiles [32]

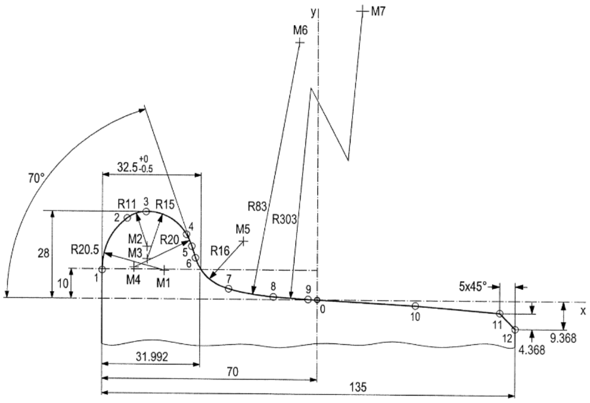
y
M7
M6
70°
32.5 +0 -0.5
R11
3
R15
2
R83
R303
4
M5
M2
R20
28
R20.5
M3
5
R16
6
1
M4
M1
10
7
8
9
5x45°
0
10
x
11
12
9.368
4.368
31.992
70
135

Figure 3.9: ORE S1002 wheel profile [33]

Table 3.2: Unit system

Parameter	Unit
Length	mm
Mass	t
Force	N
Time	s

3.3.2 Materials

Since the plasticity behavior of the steel is essentially not a primary factor in the instability behavior of the wheel-rail system, the non-linear behavior of the materials used in the analysis is not considered. Therefore, all the materials are considered linear-elastic. The steel constituting the wheelset and the rails is considered to be the same. Two materials are defined in the model: *steel* for the wheelset and the rails, and *concrete* for the mono block sleepers. The materials properties are depicted in Table 3.3. It is worth to underline that ABAQUS doesn't have a predefined unit system. All the values must be consistent with a chosen unit system. The output parameters values will be consistent with the unit system chosen. The chosen unit system is depicted in Table 3.2. In order to assess the consistency of a unit system, usually one can use Newton's second law as verification check.

$$F = ma$$

$$[N] = \rho V a = \frac{[t]}{[mm]^3}[mm]^3[a]$$

$$[Kg]\frac{[m]}{[s]^2} = \frac{[Kg]}{1000}[a]$$

Therefore, the acceleration unit is:

$$[a] = \frac{[mm]}{[s]^2}$$

With the selected unit system, the composed units are subsequently defined as follows:

- Density: $[t/mm^3]$
- Frequency: $[Hz]$ $[1/s]$
- Acceleration: $[mm/s^2]$
- Stress: $[Mpa]$ $[N/mm^2]$

3.3.3 Assembly

Parts

As preliminary work, it is necessary to model the solid parts constituting the assembly and to assign them the related material pieces of information. Moreover, both rails

Table 3.3: Materials parameters

Type	Density $[t/mm^3]$	Young Modulus [MPa]	Poisson's ratio [-]
Steel	7.85e-9	206000	0.3
Concrete	2.4e-9	30200	0.2

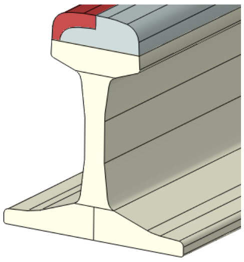

Figure 3.10: High rail sub-domains for mesh refining

and wheels are divided into sub-domains, i.e. different geometrical parts to be tied together, for the purpose of refining the mesh near the contact area (see Chapter 3.3.5).

Rails One first parameter to consider is the curvature of the rails in the selected curved track. For the purpose of the CE analysis only, it is not strictly necessary to consider and could be neglected. However, the model is meant to be ready to perform dynamic analysis as well, therefore also this nonlinear geometric parameter is considered in the model. The optimal length of the rail track model is a nontrivial issue since it can change the dynamic properties of the track. Hence, in order to choose the track length the effect of this parameter on the dynamic properties of the track is studied. For more informations, see Chapter 3.4. The rails solid geometries are modeled by means of three geometrical sub-domains:

- Rail foot and web;
- Rail head;
- Rail contact area;

The rails sub-domains can be defined by using a revolution extrusion with respect to the track curve center. The approximated extrusion angle can be computed as follows:

$$\alpha = \frac{l}{\rho} \tag{3.3.1}$$

Where l is the rail track length and ρ is the curve radius. The inclination angle, which is set to 1/20, must be considered before the solid extrusion of the rails.

Since the contact position in the low rail and in the high rail is different on the leading wheelset in the curved steady-state condition (see Chapter 3.1), the partition strategy will take into consideration different rail sub-domains on the low rail and on the high rail. In Figure 3.10 are depicted the geometrical sub-domains for the high rail.

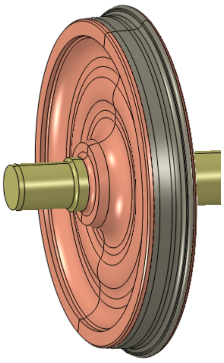

Figure 3.11: European wheelset sub-domains for mesh refining

Wheelset The internal distance between the flanges of the wheels is standard, i.e. 1360 mm. The wheelset solid geometry is instead modeled by means of three geometrical sub-domains:

- Wheelset axle;
- Wheelset wheels;
- Wheelset rim;

The solid wheelset sub-domains are straightforwardly obtained by using a complete revolution extrusion (360 degrees) with respect to the axle axis.

In Figure 3.11 are depicted the geometrical sub-domains for the European wheelset case.

Sleeper The JBV60 sleepers are modeled starting from the technical draw depicted in Figure 3.8. The modeling process started by using an extrusion block and by deploying several features available in the part modeling section of ABAQUS up until the final geometry is obtained.

Assembly

The low rail and the high rail are placed at a relative distance equal to the set gauge. A master sleeper is positioned at $\sim 300mm$ from the rails boundaries by using a radial displacement with respect to the curve center (see Eq. 3.3.1). All the other sleepers are modeled by radially patterning the master sleeper with respect to the curve center and by considering a relative distance equal to the set sleeper spacing. The standard values for the gauge and the sleeper spacing are 1435mm and 600mm respectively. The cant is considered by rotating all the sleepers with a rotation axis coincident to the low lateral edge of the sleepers on the low side of the curve of an approximated angle equal to:

$$\beta = arctg\left(\frac{c}{h}\right)$$

where c is the cant and h is the lateral distance between the rotation axis and the high rail head. The rails are constraint to have the low face of their rail foot parallel to the sleepers faces.

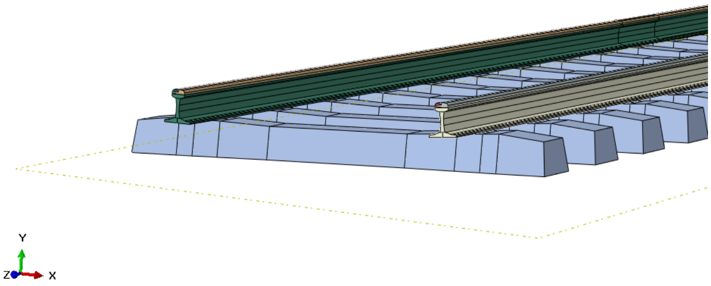

Figure 3.12: View of the assembled track model

Figure 3.12 shows a view of the model of the track assembled.

The wheelset is positioned in the longitudinal central region of the rail track model. In order to position correctly the wheelset on the global assembly, it is necessary in the first place to position it in a centered position, i.e. with the axle axis parallel to the lateral direction of the nearest sleeper and laterally centered with respect to the rail track. Then, by using the MBS results (see Chapter 3.1) it is possible to position the wheelset in the reference position by applying the roll angle and the yaw angle of the wheelset.

The final wheelset position has to consider the contact initialization between wheels and rails, as well as the initialization of the steady state suspension forces acting on the bearings. Therefore, several ABAQUS static steps are necessary. From the assembly point of view only, the wheelset is placed with the contact surfaces of the wheels a few millimeters distant from the railheads ones. The wheel in contact with the high rail is placed in order to have the smallest distance as possible between the contact profile flange and the railhead, with an approximated position in accordance to the MBS contact angle results.

3.3.4 Interactions

Tie Interactions

As previously mentioned, in order to refine the mesh near the contact area the geometries of the rails and of the wheelset are divided into sub-domains to mesh separately. However, in order to deal with a single solid body *tie couplings* need to be defined among the sub-domains interfaces. According to [21], a tie constraint ties two separate surfaces together so that there is *no relative motion* between them.

Contact interaction

The contact interaction between the wheels and the rails is defined only near the contact region in order to reduce the computational effort of the simulation. The surfaces used in the contact definition are the ones defined by the standard partitions of the rail and of the wheels created during the meshing refining stage (see Chapter 3.3.5). The slave surfaces are considered to be the rails ones.

The contact interaction is defined as follows: the *sliding formulation* is Finite sliding, the *Discretization method* is Surface-to-surface and there is no *slave adjustment*, since no overclosure between the master and slave surfaces is present.

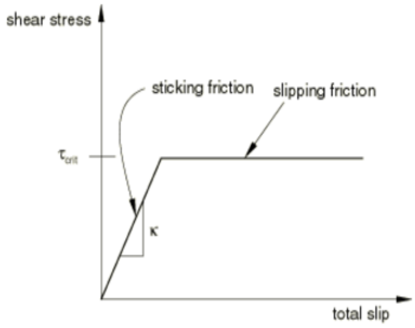

Figure 3.13: Tangential contact behaviour [21]

Only purely mechanical contact properties are considered. The contact model is supposed to have only a *normal* and *tangential* behaviors.

The *Normal behavior* has as *Constraint enforcement method* the Penalty method, while as *Pressure-Overclosure relationship* the standard *Hard Contact* (see Chapter 2.3.3).

The *Tangential behavior* considers a simplified model with respect to the theories in Chapter 2.3; it considers a classical Coulomb friction model ($\tau = \mu N$) for a sufficiently high total contact slip, and an elastic slip ($\tau = \mathcal{K}\xi$) for small values of contact slip, in order to take into account the contact sticking creepage.

Figure 3.13 depicts the tangential contact model considered in the analysis. The maximum allowable shear stress, τ_{crit}, depends on the friction coefficient chosen. Further nonlinearities, such as the dependence of the friction coefficient on the slip rate or on the contact normal pressure, are not considered.

Couplings

In order to apply the primary suspension forces, it is necessary to define two interface nodes by coupling two reference points on the axle surfaces corresponding to the bearings position. Among the different coupling types available in ABAQUS, the *kinematic coupling* is used. A kinematic coupling constrains the motion of the coupling nodes (the mesh nodes belonging to the coupling surface) to the rigid body motion of the reference node [21]. In general, the constraint can be applied to user-specified degrees of freedom. In this case, all degrees of freedom are constrained.

Rail pad Modeling

Depending on the type of application of the model, the rail pad can be modeled in several ways. What changes between the different model strategies is basically the detail level. According to [34], the rail pad can be modeled either by means of concentrated springs and dashpots or by means of a solid rail pad modeling.

The major modeling strategies are [34]:

- *Line-SD model*: The rail pad is mainly represented as one pair of linear spring and viscous damper in parallel. In a 3D FE model, a single SD pair would make the rails unstable [34]; therefore, a line of SD pairs along the rail width are used.
- *Area-SD model*: The rail seat is covered with multiple discrete linear SD pairs.

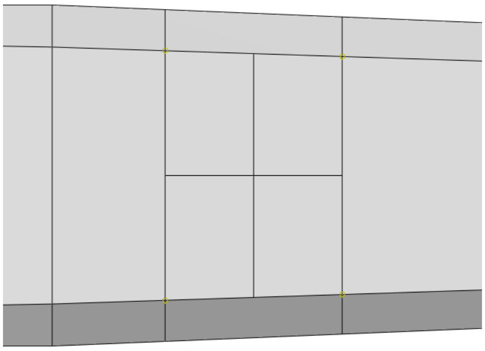

Figure 3.14: Cross-shaped sleeper surface partition

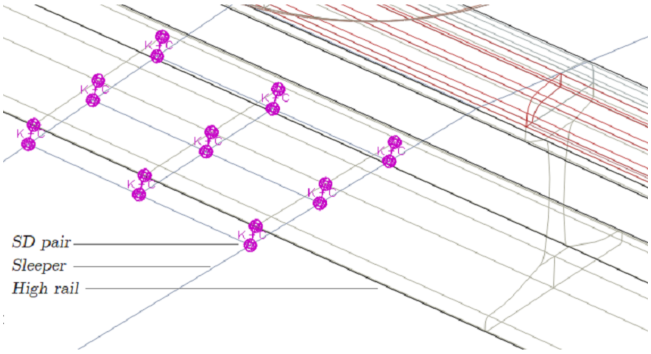

Figure 3.15: Railpad model

- *Solid-connected model*: The rail pad is represented by elastic solid elements covering the entire rail seat; Rayleigh damping is considered; the surfaces are tied to the rail and to the sleeper.

- *Solid-contact model*: As the Solid-connected model, except that in this case the model considers the clamping forces and the contact interaction between the rail pad and the rail and sleeper.

The Area-SD model is used in order to model the rail pads in the rail track model. A set of nine SD pairs is considered to be sufficient for modeling the rail pad effect in the frequency range of interest [0-1200Hz].

SPRING2 and DASHPOT2 types are used in order to model SD pairs between two nodes. The relative displacement across an SD element is the difference between the ith component of displacement of the SD pair first node and the jth component of displacement of the SD pair second node, where i and j are directions defined by the user [21].

In order to define the connecting nodes, the faces of the sleepers and of the rails in contact with the pad are partitioned by properly projecting the rails and sleepers surfaces' edges.

The nodes placed in the center are obtained by further partitioning the surface with a cross-shaped sketch, as shown in Figure 3.14.

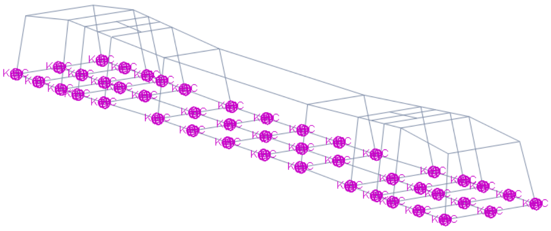

Figure 3.16: Ballast model

In order to make the definition of all the SD pairs on the model faster, a *Phyton* script is necessary. In the first place, two sets of nodes are defined: one for the sleepers and one for the rails. After that, the sets are used in the script for cycling the creations of spring-dashpot connections. Figure 3.15 depicts the pad model considered in the analysis.

Ballast modeling

In the same way the rail pads are modeled, ballast is modeled by using the Area-SD Model approach. In this case, SPRING1 and DASHPOT1 spring-dashpot connection types are used, since, in the case of ballast, the connection must be between a set of nodes and the ground. The relative displacement across an SD element is, in this case, the i-th component of displacement of the spring's node, where i is defined by the user [21]. Also, in this case, a *phyton* script is used in order to define all the connections. A series of node sets are created, including all the geometrical vertices of the bottom surfaces of the sleepers.

Figure 3.16 depicts the ballast model according to the Area-SD model approach.

3.3.5 Mesh

The resolution of the wheel-rail interface has a strong impact on the complex eigenvalue analysis results; therefore, a sufficiently accurate contact distribution has to be considered in the analysis. The mesh is hence refined as much as possible near the contact region. As discussed in Chapter 3.3.3, since the stress distribution accuracy is not needed for the purpose of this analysis, the geometries can first be divided into sub-domains in order to define regions with remarkably different mesh sizes. The connecting surfaces of the sub-domains constitute a discontinuity on the mesh. Therefore, they must be placed far enough from the contact region in order to not affect the results.

Several geometry partitions have been made. The rails' sub-domains comprising the foot and web are partitioned into three parts: the rail foot, the rail web and the low rail head. The rails are also partitioned longitudinally of a sleeper span length starting from the midspan near the wheelset-rails contact region, in order to further refine the mesh near the contact area.

The sub-domain of the wheelset rim is partitioned radially of an angle equal to 20 *deg*.

The global seed size is 35 mm. Furthermore, both the wheels and rails contact partitions have a double biased longitudinal seed distribution with a maximum size

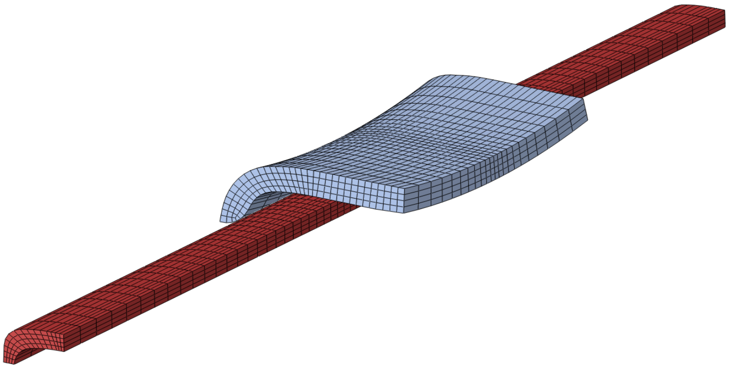

Figure 3.17: Mesh of contact partitions at the high rail side

of 15 mm far from the contact region and a minimum size of 4 mm near the contact region.

The partitions of the rail head and the contact sub-domains, as well as the rail foot are meshed with the *Advancing front* algorithm. The partitions of the rail web and the rail head below the gauge face are meshed with the *Sweep* algorithm.

All the wheelset sub-domains and partitions are meshed by means of the *Sweep* algorithm.

The sleepers are straightforwardly meshed by means of the *structured* meshing technique.

The final mesh size near the contact region used in the analysis is ca. 4x4x4 mm both in the rails and the wheelset.

Figure 3.17 depicts the mesh configuration for the contact partitions in the wheelset and rail at the high rail side.

Since the analysis is a linear perturbation in frequency domain, with an 8-node linear brick reduced integration elements (C3D8R) mesh, even with an hourglass control the analysis is highly affected by hourglass unstable zero energy modes detection.

For this reason, 8-node linear brick, *incompatible modes* elements (C3D8I) are used. This particular kind of element is an improved version of the C3D8-element. In particular, shear locking is removed and volumetric locking is much reduced. This is obtained by supplementing the standard shape functions with the so-called *bubble functions*, which have a zero value at all nodes and non-zero values in between. Even though the best quality is generally obtained with quadratic elements (C3D20 & C3D20R), the C3D8I elements generally give much more quality than C3D8R elements and reduce at minimum hourglass issues.

The global model is composed of 316397 C3D8I elements.

3.4 Track Dynamic Properties

In order to assess the qualitative reliability of the FE model, it is useful to simulate in the first place the vertical dynamic properties of the track in terms of rail vertical receptance.

Moreover, as discussed in Chapter 3.3.3, since the real structural system has a longitudinal length that can be considered infinite, and since a relatively long rail track model is unfeasible to be used because it would lead to significant computational efforts, the model will always have a certain degree of approximation with respect to the real track dynamic properties. A trade-off analysis between rail track length, dynamic properties accuracy and computational effort is necessary. Hence, the effect of the track longitudinal length on the vertical rail receptance has been studied in order to set the optimal track length of the FE model. This has been done by computing the track FRF for different lengths of the model, looking for a threshold level above which the convergence of results is achieved.

3.4.1 Track Receptance

In order to perform the analysis, an auxiliary straight track model is used. The model doesn't consider rail curvature and cant, while the assembly and meshing procedure is the same as the one discussed in Chapters 3.3.3 and 3.3.5. The wheelset is not assembled in the model. Only the vertical rail receptance is considered in the analysis, as well as only its computation in the midspan, i.e. in between two sleepers. ABAQUS makes it possible to compute the *frequency response function* (FRF) of a structure subjected to a sinusoidal load. First, a *natural frequency extraction* in the frequency range of interest [0-2000 Hz] is performed. Afterwards, a *Steady-state modal dynamics* is performed in the same frequency range.

A unitary vertical concentrated force is applied in correspondence of a reference node in the midspan in the middle of the track model. The rails are hinged at their end. A node set comprising eleven nodes in the same midspan area is defined in order to reduce singularities in the final response function by taking the average of the receptance responses at each node.

A preliminary model with a track length of 36000 mm, which in general is considered as standard length, was first considered. This led to an extremely slow computational time. Hence, three different track lengths are considered in the analysis: 4200 mm, 7800 mm and 11400 mm, corresponding to models of 7, 13 and 19 sleeper spans. The structural parameters used for this analysis are the ones of the *2-4* case (see Table 3.9 in Chapter 3.6).

3.4.2 Track length effect on dynamic properties

The computed vertical track receptances are depicted in the bi-logarithmic plot in Figure 3.18. The typical track resonances are clearly visible: at around 80 Hz the P2 resonance peak is present, while around 1200Hz the pinned-pinned resonance peak is visible as well. It can be clearly seen that the vertical response of the track model of length 4200 mm is highly affected by the short track length. Several resonance peaks due to hinge boundaries effect on the system dynamics are present, making it unfeasible to be used for the global analysis.

As the rail track model length increases, the effect of boundaries fades out leaving only the unaffected vertical dynamics.

Figure 3.19 depicts the trend of the pinned-pinned resonance frequency with respect to the rail track longitudinal length. The frequency at short track lengths is clearly higher because of the increase of the stiffness due to the effect of boundaries. The frequency ranges from 1137 Hz ca. at 4200 mm to 1085 Hz ca. at 11400 mm. After a track length of 7800 mm, the frequency converges, meaning that the effect of boundaries becomes less prominent.

The track model of length 11400 mm is considered to be sufficiently unaffected by boundaries effect in the frequency range of interest for performing the global complex

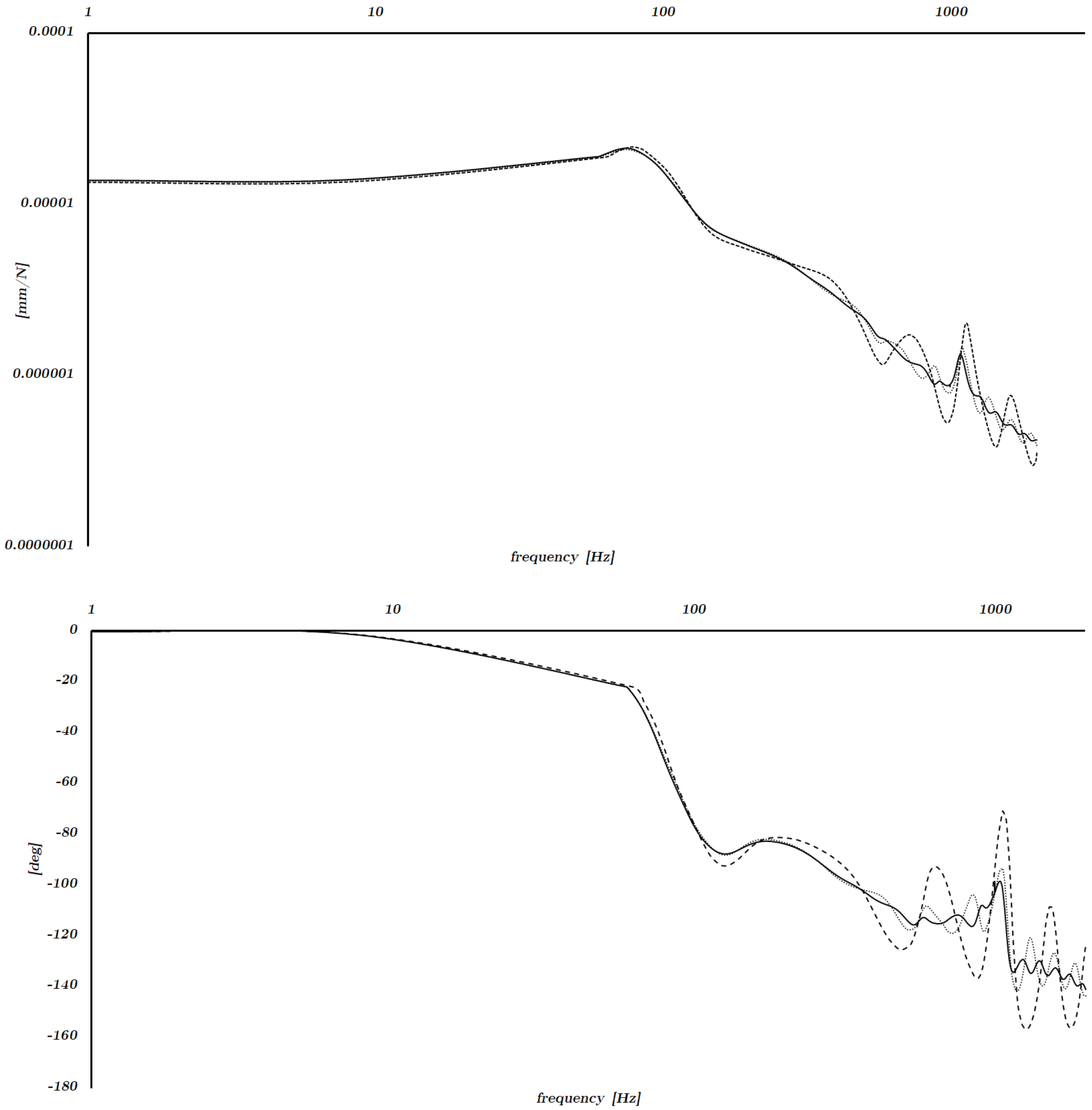

Figure 3.18: Vertical midspan track receptance functions a) Magnitude [N/mm] b) Phase [deg]; (- - -) Rail length: 4200 mm (······) Rail length: 7800 mm (——) Rail length: 11400 mm

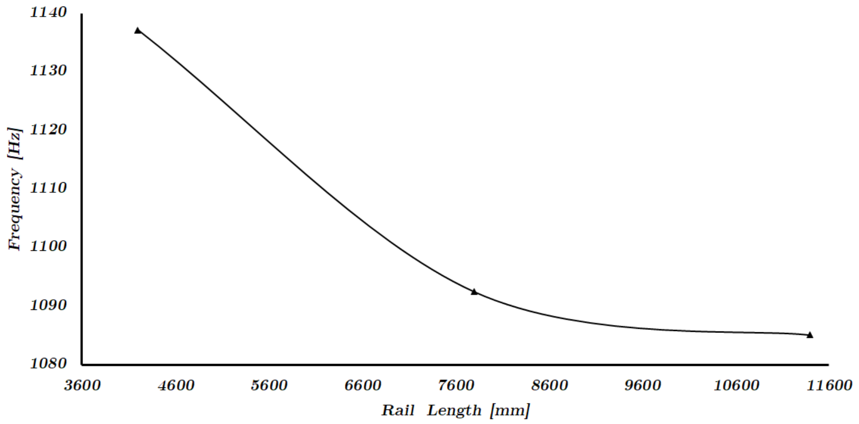

Figure 3.19: Convergence of the pinned-pinned resonance frequency

eigenvalue analysis.

Therefore, a rail track model of length 11400 mm, i.e. 19 sleeper spans, is used.

3.5 C.E. Analysis preliminary settings

According to the literature, in order to perform a complex eigenvalue analysis four main steps are required as follows:

1. *Nonlinear steady-state analysis* of the wheelset-track system for applying the suspension forces on the bearings;
2. *Nonlinear steady-state analysis* for imposing the sliding speed on the wheelset;
3. *Natural frequency extraction* of the system without considering the friction coupling and damping to find the projection subspace;
4. *Complex eigenvalue extraction* of the system that incorporates the effect of the friction coupling and damping;

The suspension forces applied in the first static procedure come from the steady-state dynamic condition of the preliminary MBS simulation. Applied to the FE model, they define the initial *Reference State* of the system, which is not affected by sliding contact. The fourth step is therefore needed for initializing the tight curved condition, here called *Sliding contact State* of the system. This is achieved by applying the lateral wheelset velocity and therefore by considering near saturation lateral creep forces in the analysis.

The necessary analysis steps are hence schematized in the flowchart depicted in Figure 3.20.

3.5.1 Analysis steps

The definition of the analysis steps in ABAQUS follows the necessary steps for performing a complex eigenvalue analysis defined previously. However, since with a single static step for the suspension forces definition divergence has been experienced during

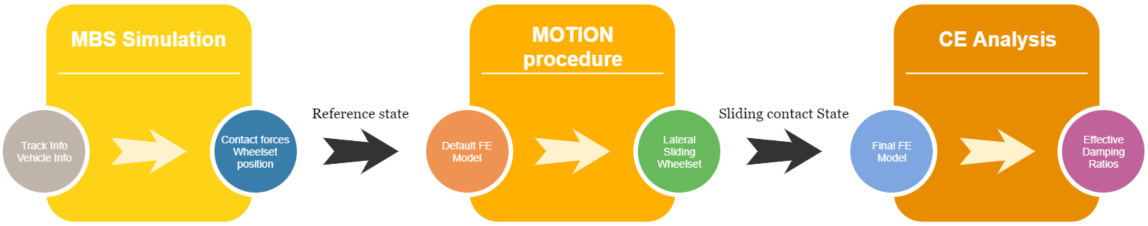

Figure 3.20: Step flow of the analysis

Table 3.4: ABAQUS analysis steps

Name	Procedure
Contact Initialization	Static, General
Vertical suspension forces initialization	Static, General
Lateral suspension forces initialization	Static, General
Sliding initialization	Static, General
Natural frequency extraction	Frequency
CE extraction	Complex frequency

the contact initialization between wheelset and rails, a preliminary static step is considered with the only purpose of initializing the contact between the bodies, as well as the suspension forces initialization step is divided into two separate static procedures for the vertical forces definition and for the lateral forces definition.

The steps composing a single complex eigenvalue extraction of the analysis are described in Table 3.4. All the static procedures have a time period set equal to 0.1 s. A nonlinear geometry procedure (Nlgeom) is considered. In order to avoid solution divergence, the initial increment size is set equal to 0.005 s, leaving an automatic incrementation type.

In the *Natural frequency extraction* step, the *Lanzcos* Eigensolver is considered. A nonlinear geometry (Nlgeom) is considered. The minimum and maximum frequencies of interest are set equal to $0.1 Hz$ and $1300 Hz$, respectively. The maximum number of eigenvalues requested is set equal to 1500. The eigenvectors are normalized by mass.

In the *CE Analysis* step the minimum and maximum frequencies of interest are set equal to $0.5 Hz$ and $1000 Hz$, respectively. The maximum number of eigenvalues requested is set equal to 1200. A nonlinear geometry (Nlgeom) is considered.

3.5.2 Loads & Boundary conditions

Table 3.5 depicts the loads and boundary conditions definitions along the analysis procedures.

In the *initial* step, Rail Hinges BCs and Bearings BCs are defined. In the former, the rail transversal surfaces are *pinned* ($U1 = U2 = U3 = 0$). In the latter, the bearings surfaces' coupling points are constrained ($U3 = UR1 = UR2 = UR3 = 0$). U1 & U2 are left free. For simplicity, also the wheelset rotation about its axis has been assumed constrained.

In the *Contact initiation* step, a Contact Initiation Displacement has been applied on the bearings surfaces' coupling points ($U1 = 3mm; U2 = -4mm$).

In the *Vertical suspension forces initiation* step, the vertical suspension forces are

Table 3.5: ABAQUS Loads & Boundary conditions

	1 Initial	2 Contact Initiation	3 Vertical suspension forces initiation	4 Lateral suspension forces initiation	5 Sliding Initiation	6 Natural frequencies extaction	7 CE extraction
High bearing suspension forces	-	-	Created	Modified	Propagated	Built into base state	Built into base state
Low bearing suspension forces	-	-	Created	Modified	Propagated	Built into base state	Built into base state
Rail Hinges BCs	Created	Propagated	Propagated	Propagated	Propagated	Propagated from base state	Built into modes
Bearings BCs	Created	Propagated	Propagated	Propagated	Propagated	Propagated from base state	Built into modes
Bearings BCs deformed shape	-	-	-	-	Created	Propagated from base state	Built into modes
Lateral slip	-	-	-	-	Created	Propagated from base state	Built into modes
Contact initiation	-	Created	Modified	Inactive	-	-	-

applied as concentrated loads on the bearings surfaces' coupling points. At the same time, the vertical contact initiation displacement is suppressed.

In the *Lateral suspension forces initiation* step, the lateral suspension forces are applied as concentrated loads on the bearings surfaces' coupling points. At the same time, the lateral contact initiation displacement is suppressed.

In the *Sliding Initiation* step, the Bearings BCs on the deformed wheelset and the Lateral wheelset slip are defined. In the former, a Velocity boundary condition is applied on the bearings surfaces' coupling points ($V1 = V2 = 0$). In the latter, the lateral wheelset sliding condition is achieved by modifying the analysis input file by considering a motion procedure:

$$\begin{aligned} *MOTION, TRANSLATION \\ TYPE = VELOCITY \\ Wheelset, 1, , V_{lateral,1} \\ Wheelset, 2, , V_{lateral,2} \end{aligned}$$

where $Wheelset$ is a node set comprising all the nodes defining the wheelset, and $V_{lateral,1}$ and $V_{lateral,2}$ are the components of the lateral wheelset velocity.

As long as the lateral creep forces are saturated, the wheelset lateral translation magnitude value is not relevant. The lateral sliding speed of the leading wheelset is equal to

$$V_{lateral} = V sin\psi$$

where V is the forward vehicle speed and ψ is the wheelset angle of attack. From the MBS results (see Chapter 3.1) the angle of attack can be defined.

3.6 Design of Experiments (DOE)

In order to design an experiment that could be able to answer the research questions of this thesis (see Chapter 1.4), it is useful to investigate how various typical parameters of the wheelset-track system might affect the corrugation occurrence in a tight curved condition in terms of variation of a predefined corrugation index. This chapter is a brief introduction to how the conducted experiment has been designed.

Generally, the relevant variables of a process (*factors*) are accurately chosen in order to observe the effect their changes have on one or more response variables (*outputs*). The *design of experiments* (DOE) is an efficient procedure for planning experiments and analyze the results giving valid and objective conclusions [35].

Every cause-effect process can be modeled by using a simple 'black box' diagram, with several discrete or continuous *input factors* that can be controlled in the analysis, several discrete or continuous *input co-factors* that are not controllable during the experiment and several continuous *outputs*, as shown in Figure 3.21.

During an experiment design, one has, first of all, to determine which is the main *objective* of the analysis. Different objectives are associated with different experimental designs. Common experiment objectives are for instance choosing between two factors in spite of the existence of other factors (*comparative*) or selecting the few important main effects from the many less important ones (*screening*). At the same

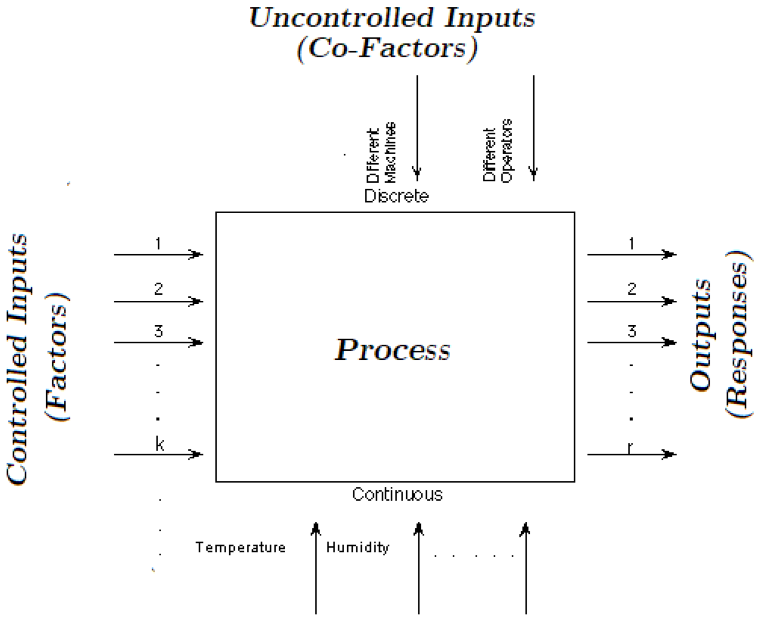

Figure 3.21: *Black box* process model type [35]

time, the process variables, which include both factors and outputs, and the number of *levels* for each variable have to be chosen. Variable levels are the discrete possible values that variables can assume during the analysis. Once the experiment design, the process variables, and their levels are defined, the numerical simulation runs can be performed and the results analyzed by means of statistical approaches.

3.6.1 Parameters

Among the structural and geometrical parameters of the coupled wheelset-track system, the analysis is focused on four main factors that might affect the corrugation formation:

- *Pad Stiffness*: Pad stiffness is considered in corrugation literature as one of the parameters that can be modified in order to inhibit corrugation occurrence. A numerical study conducted in 1998 by *H. Ilias* [36] and experimental pieces of evidence collected in a study conducted in 2005 by *J. Vinolas* [37] found that stiffer rail pads lead to higher corrugation growth.
- *Vertical Ballast Stiffness*: The ballast structural properties is in this analysis considered as a potential factor of corrugation influence.
- *Wheelset Design*: As discussed in Chapter 3.3.1, two different wheel geometries are used. This factor might have a strong impact on the unstable mode shapes properties and hence inhibit corrugation formation.
- *Rail Gauge*: Rail gauge is a geometrical parameter that defines the lateral distance between the rails (see Chapter 2.2.1). In curved tracks, rail gauge is widened in order to have a better bogie dynamics. Table 3.6 depicts the Italian gauge widening standard. The variation from a gentle curve to a very tight one

Table 3.6: Italian gauge widening standard [38]

Curve Radius [m]		Gauge [mm]
From	To	
∞	275	1435
<275	250	1440
<250	225	1445
<225	200	1450
<200	175	1455
<175	150	1460
<150		1465

Table 3.7: Analysis factors

Factor		High	0	Low
Vertical Pad Stiffness, $K_{pad,v}$	[MN/m]	600	340	80
Vertical Ballast Stiffness, $K_{ballast,v}$	[MN/m]	200	110	20
Wheelset Design, d	[-]	European		Chinese
Rail Gauge, g	[mm]	1455		1435

is circa 30 mm. This factor can change the position of the contact points on the rail and wheel surface, the contact parameters and hence change the instability occurrence.

The analysis is hence composed of four factors and one output. The *Wheelset Design* is by its very nature a two-level factor. The *Rail Gauge* is chosen to be a two-level factor as well, while the Vertical Pad Stiffness and the Vertical Ballast Stiffness are chosen to be three-level factors because of their wide variation range.

Table 3.7 depicts the chosen factors levels. The Rail Gauge factor ranges from a standard value to a high value that corresponds to a tight curve radius between 175m and 200m considering the Italian standard. It is, however, useful to remark that the curve radius is not considered a variable in the analysis.

Table 3.8 depicts the remaining structural parameters of the system, which are left constant along the analysis. The pad stiffness levels range, as well as its constant structural parameters, are determined from a paper published by Ki. Knothe and S.L. Grassie [39], while the ballast stiffness levels range and structural parameters are determined from the studies published by the *EUROBALT project* [40].

The lateral and longitudinal stiffness of the pad and ballast are considered to be equal. The lateral pad stiffness is related to the vertical one by the following relation:

Table 3.8: Structural Parameters of the system

Parameter		
Vertical Pad Damping, $C_{pad,v}$	[MNs/m]	0.03
Lateral Pad Damping, $C_{pad,l}$	[MNs/m]	0.032
Lateral Ballast Stiffness, $K_{ballast,l}$	[MN/m]	55
Vertical Ballast Damping, $C_{ballast,v}$	[MNs/m]	0.1
Lateral Ballast Damping, $C_{ballast,l}$	[MNs/m]	0.05

$$K_{pad,l} \simeq 0.2K_{pad,v}$$

3.6.2 DOE cases

The experimental analysis chosen is a *multilevel full factorial design*. All the combinations of the factors levels are considered in the analysis, hence leading to a total of 36 runs. This design type is useful for performing screening analysis, i.e. for analyzing which are the factors that most influence the output variable.

Table 3.9 lists all the DOE cases considered in the analysis.

3.7 Corrugation Index

The effective damping ratio δ is not sufficient to be used as corrugation index. It needs also to be considered the potential slip at the contact patch that can be generated by the unstable modes. Therefore, the *Effective Corrugation Index* (γ) is computed as:

$$\begin{cases} \gamma_k = 0 & \text{if } \delta_{k,min} > 0 \\ \gamma_k = \frac{\sum\limits_{i=1}^{N} |\delta_i| \xi_i}{\xi_0} & \text{if } \delta_{k,min} < 0 \end{cases} \tag{3.7.1}$$

where k is the case considered, N is the number of unstable modes detected in the considered case, δ_i is the ith unstable mode *effective damping ratio*, ξ_0 is a normalization factor equal to 10^{-6} and ξ_i is the ith slip factor computed as

$$\xi_i = \sqrt{(u_{1w,i} - u_{1r,i})^2 + (u_{3w,i} - u_{3r,i})^2}$$

where u is the mean nodal normalized displacement of the unstable mode shape near the contact patch, in the transversal direction (1) and longitudinal direction (3) for the low wheel (w) and the low rail (r). The mean nodal normalized displacements are computed as an average value of the relative displacement of the mode shape on five different nodes in the contact region. In this way, the effective damping ratio δ_i is used as instability index of the ith mode, and ξ_i is used as slip index of the ith mode.

Table 3.9: DOE cases

Run Index	*Gauge* [mm]	*Wheelset design* [-]	$K_{pad,v}$	$K_{ballast,v}$
1-1	1435	European	80	20
1-2	1435	European	80	110
1-3	1435	European	80	200
1-4	1435	European	340	20
1-5	1435	European	340	110
1-6	1435	European	340	200
1-7	1435	European	600	20
1-8	1435	European	600	110
1-9	1435	European	600	200
1-10	1435	Chinese	80	20
1-11	1435	Chinese	80	110
1-12	1435	Chinese	80	200
1-13	1435	Chinese	340	20
1-14	1435	Chinese	340	110
1-15	1435	Chinese	340	200
1-16	1435	Chinese	600	20
1-17	1435	Chinese	600	110
1-18	1435	Chinese	600	200
2-1	1455	European	80	20
2-2	1455	European	80	110
2-3	1455	European	80	200
2-4	1455	European	340	20
2-5	1455	European	340	110
2-6	1455	European	340	200
2-7	1455	European	600	20
2-8	1455	European	600	110
2-9	1455	European	600	200
2-10	1455	Chinese	80	20
2-11	1455	Chinese	80	110
2-12	1455	Chinese	80	200
2-13	1455	Chinese	340	20
2-14	1455	Chinese	340	110
2-15	1455	Chinese	340	200
2-16	1455	Chinese	600	20
2-17	1455	Chinese	600	110
2-18	1455	Chinese	600	200

Chapter 4

Results

As previously discussed in Chapter 2.5, the results of the analysis are given in terms of complex eigenvalues and complex eigenvectors, i.e. mode shapes, in the frequency range of interest and their associated effective damping ratio.

Figure 4.1a depicts the typical distribution of the complex eigenvalues of the system in terms of effective damping ratio in the frequency range of interest [0-1000Hz]. The particular distribution is related to the case *2-4* of the analysis. As one can readily see, almost all the effective damping ratios detected are positive, such that their associated eigenvalue is stable. Hence, no vibration at that particular frequency and mode shape occurs. Figure 4.1b gives more emphasis to the near-zero effective damping ratios. Two negative effective damping ratios can hence be detected in the chart. Therefore, these two factors are related to unstable vibration modes, which in turn can give rise to relatively high vibrations at those particular frequencies and a consequent fluctuation of the contact forces at the same frequency, thus leading to rail corrugation [10].

Table 4.1 shows the numerical pieces of information about the unstable modes effective damping ratios and frequencies.

Figures 4.2 and 4.3 show the mode shapes associated with the unstable modes detected in the analysis. Interestingly, one can see that a great deal of the vibration at those frequencies occurs at the wheelset, and in particular at the low wheel. It is

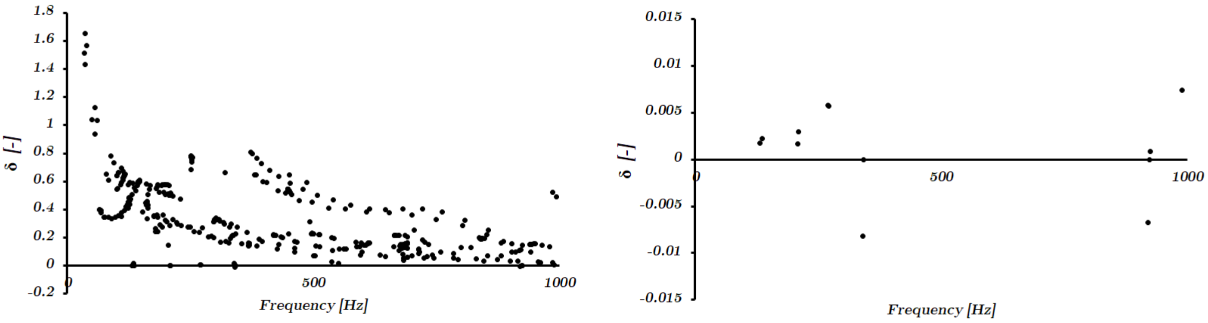

Figure 4.1: Case *2-4*: Results in terms of effective damping ratios and their relative frequency. a) General results; b) Emphasis on the unstable eigenmodes

Table 4.1: Case *2-4*: Unstable modes *effective damping ratios* and *frequencies*

Mode	δ	Frequency [Hz]
I	-0.0082	339.91
II	-0.0067	919.36

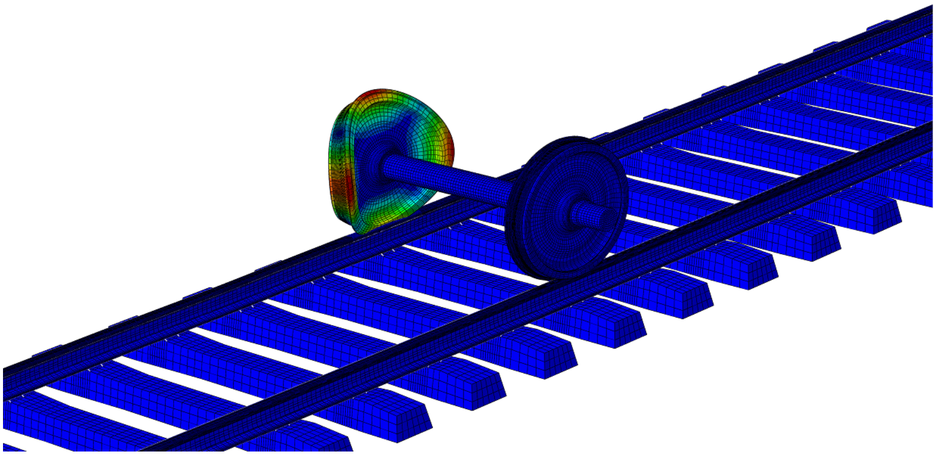

Figure 4.2: Case *2-4*, Mode I: Unstable modeshape

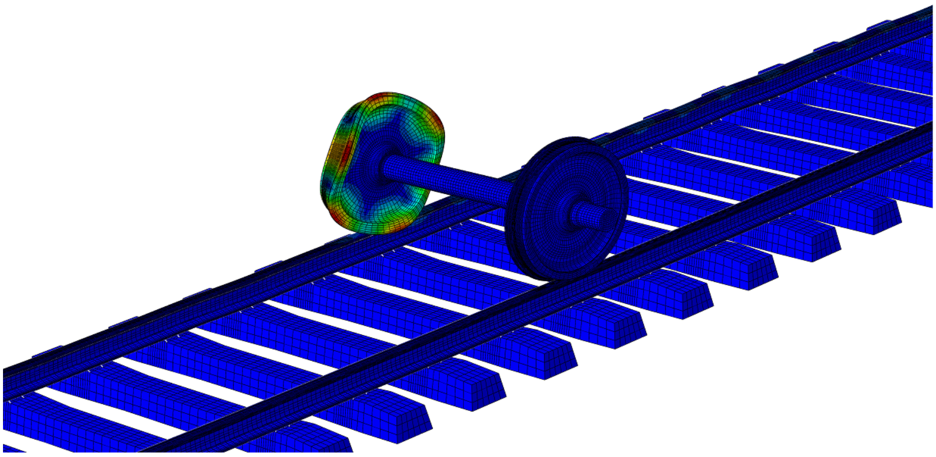

Figure 4.3: Case *2-4*, Mode II: Unstable modeshape

Table 4.2: Reference model properties

$F_{high,v}$	[N]	-103200
$F_{low,v}$	[N]	-91800
$F_{high,l}$	[N]	7640
$F_{low,l}$	[N]	7640
Yaw, ψ	[deg]	0.3
Gauge	[mm]	1435
Wheelset design	[-]	Chinese
$K_{pad,v}$	[MN/m]	78
$K_{pad,l}$	[MN/m]	29.47
$C_{pad,v}$	[MNs/m]	50
$C_{pad,l}$	[MNs/m]	52
$K_{ballast,v}$	[MN/m]	89
$K_{ballast,l}$	[MN/m]	50
$C_{ballast,v}$	[MNs/m]	89.8
$C_{ballast,l}$	[MNs/m]	40

also interesting to remark that the vibration of the low wheel mostly occurs in lateral direction. The sleepers are not participating in the vibration modes. This particular vibration displacement distribution, which can be associated with a high slip between the low rail and the low wheel and therefore to a high corrugation rate at the low rail, matches with the rutting corrugation experimental pieces of evidence that show a typical corrugation formation at tight curves on the low rail [4].

Before proceeding with running the DOE cases, a validation procedure of the model with respect to a reference literature paper has been considered.

4.1 Model Validation

The analysis has been conducted by taking as reference the literature paper *A transient dynamic study of the self-excited vibration of a railway wheel set-track system induced by saturated creep forces*, published in 2014 by *G.X. Chen et al.*, from the Tribology Research Institute of Southwest Jiatong University, Chengdu, China [10]. At first, it is useful to validate the model with respect to the reference one used in the above mentioned paper.

In order to do so, all the structural and geometrical properties of the model have been changed to the ones used by the authors of paper [10]. Also, the boundary conditions at the wheelset bearings have been changed according to the reference.

Table 4.2 depicts the numerical values of the reference model parameters.

However, the models are not identical. The rail length of the reference model is set to 36m, the sleeper geometry is different, the inclination angle is 1/40 and the mesh is different. Moreover, the modeling procedure is different.

An unstable eigenvalue has been detected in the same frequency range of the one detected by the reference model. The validation results are collected in Table 4.3. The difference between the results is 7% for the frequency of the unstable mode and 4% for its effective damping ratio. The differences are deemed to be acceptable on account of the differences in the model and the different modeling procedures and

Table 4.3: Validation comparison results

		Model	Reference model	
Frequency	[Hz]	497.7	463.6	7%
γ	[-]	-0.0225	-0.0216	4%

numerical solutions used.

Figure 4.4 depicts the mode shapes of the unstable eigenvalues detected by the compared models. There is a clear similarity between the unstable mode shapes from the two calculations. The strong similarity of the unstable mode shapes, as well as the similarity of their effective damping ratios and frequencies, can lead to the conclusion that the model used in this analysis and the model of the literature paper considered are closely linked; hence, *the conclusions of the following analysis can be thought as supported by the reference paper mentioned [10]*. Moreover, since the models have a very different rail length, one can also conclude that *the same results can be drawn with a rail model of 11400mm length instead of the classical 36000mm rail model, thus leading to a lighter computational effort*, which is compatible with running several cases as requested in the DoE exercise.

4.2 Design of Experiments results

All 36 runs previously listed in Table 3.9 have been executed in parallel thanks to the usage of the CINECA supercomputer named *MARCONI*.

For each run case the number of unstable modes detected is collected, the minimum effective damping ratio if no unstable mode is detected and the negative effective damping ratios with their associated frequency for the eventual unstable cases detected. Finally, the corrugation index is computed.

Table 4.4 depicts the analysis results. As one can readily see, most of the cases do not detect unstable cases. In particular, the cases from *1-1* to *1-9* and from *2-10* to *2-18* are all free of instability. An important conclusion can be drawn from this initial results observation: *depending on the wheelset structure and on the gauge, corrugation can be inhibited in a wide range of values of rail pad and ballast stiffness.*

A better understanding of the analysis results can be achieved by using commonly used DOE charts.

4.2.1 Effects Plots

The Main effects plot shows the average response for a given level of a factor (*High*, *0*, *Low*) for each of the studied factors. In this way, the trend of the influence of a single factor on the output variable can be determined. The interaction plots can also be determined by considering the variation of the average response of a factor due to the level of another factor.

Figure 4.5 shows the main effects plots of the four factors taken into consideration in the analysis and the interaction plots with respect to the wheelset design. The two levels factors have been interpolated by using linear functions, while the three levels factors by using quadratic functions. The main effects plot shows the influence of a

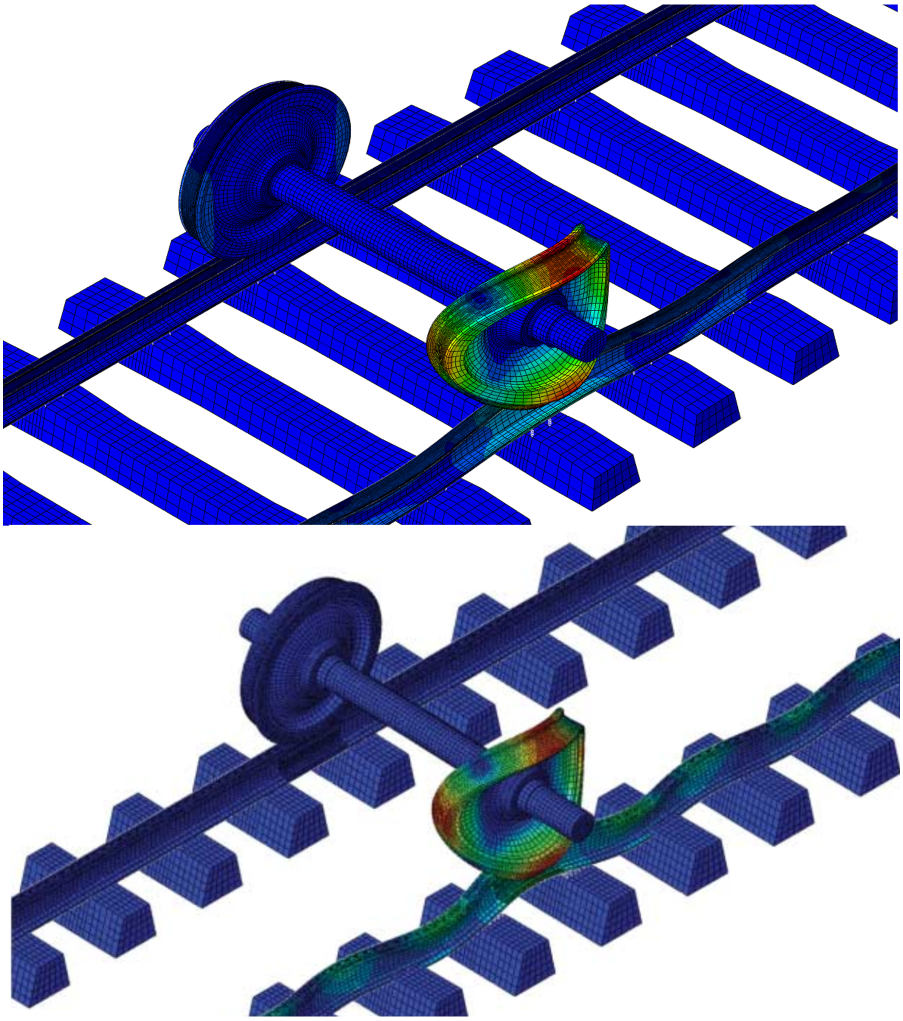

Figure 4.4: Validation comparison of the unstable modeshapes a) Novel model b) Reference paper model

Table 4.4: DOE results

Run Index	Unstable modes	Min δ	Negative δ		Frequency [Hz]		Corrugation index γ
1-1	0	0	-		-		0
1-2	0	0	-		-		0
1-3	0	0.00029	-		-		0
1-4	0	0.0007	-		-		0
1-5	0	0.0002	-		-		0
1-6	0	0.00018	-		-		0
1-7	0	0.00058	-		-		0
1-8	0	0.00065	-		-		0
1-9	0	0.00064	-		-		0
1-10	0	0.0002	-		-		0
1-11	0	0.0002	-		-		0
1-12	0	0	-		-		0
1-13	0	0	-		-		0
1-14	2	-	-0.0015	-0.018	319.38	495.59	12.5
1-15	0	0	-		-		0
1-16	0	0	-		-		0
1-17	2	-	-0.021	-0.00491	493.47	507.74	15.2
1-18	0	0	-		-		0
2-1	0	0.00046	-		-		0
2-2	2	-	-0.010	-0.0061	341.86	920.38	15.7
2-3	0	0.00038	-		-		0
2-4	2	-	-0.0082	-0.0067	339.91	919.36	11.5
2-5	2	-	-00080	-0.01	340.90	921.57	14
2-6	0	0	-		-		0
2-7	2	-	-0.0122	-0.0073	339.1	919.9	16.5
2-8	0	0	-		-		0
2-9	0	0	-		-		0
2-10	0	0.0002	-		-		0
2-11	0	0.0002	-		-		0
2-12	0	00002	-		-		0
2-13	0	0.0001	-		-		0
2-14	0	0.0001	-		-		0
2-15	0	0	-		-		0
2-16	0	0	-		-		0
2-17	0	0.0001	-		-		0
2-18	0	0.0001	-		-		0

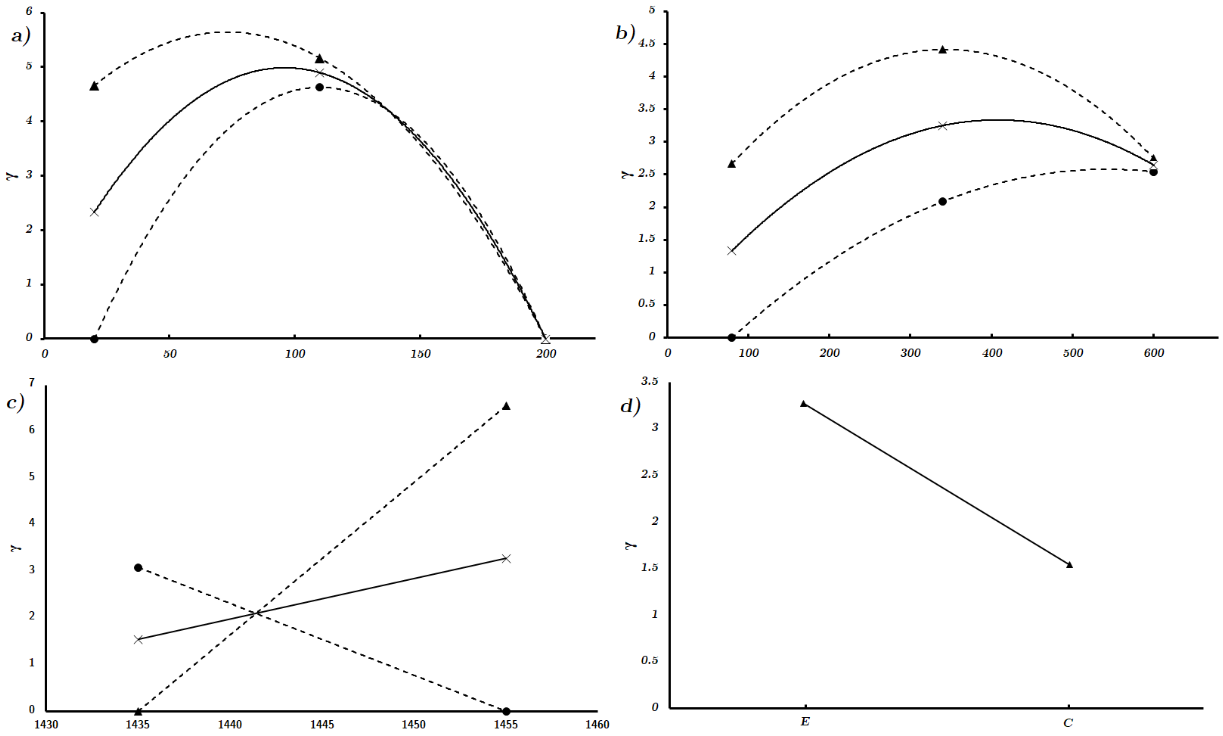

Figure 4.5: Effects plots and interaction plots with respect to the wheelset design: a) Vertical ballast stiffness [MN/m]; b) Vertical railpad stiffness [MN/m]; c) Gauge [mm]; d) Wheelset design [-]. (——): Main effects; (- - -●): Wheelset design: Chinese; (- - -▲): Wheelset design: European

single factor with respect to the full range of variation of the remaining factors of the analysis.

From these charts, one can make several conclusions:

- The main effect of rail gauge and wheelset structure is not relevant neither numerically nor statistically. This means that *taken alone, these factors are not general inhibitor parameters of rail corrugation*;
- *The vertical ballast stiffness has a maximum level of rail corrugation at a medium stiffness value, i.e.* $110 MN/m$;
- *The rail pad stiffness has a minimum level of rail corrugation for a low stiffness value, i.e* $80 MN/m$; This result is in accordance with most of the literature on rail corrugation ([4], [37], [36]).

However, considering an interaction effect of both *Gauge* and *Wheelset design*, one can detect a strong influence on rail corrugation. Figure 4.5c shows the above mentioned interaction effect. From the plot, one can conclude that:

- Considering a single wheelset design, *there is a gauge level at which corrugation is inhibited*;
- The *rate of variation* of the corrugation formation with respect to the gauge *greatly depends on the wheelset design*;

For instance, in the case of European wheelset design, the system is affected by unstable modes only for widened rail gauges, specifically for a rail gauge of 1455 mm.

4.2.2 Pareto Chart of Effects

The Pareto chart of effects, or simply *effects plot*, gives a graphical representation of the importance of each factor by showing their absolute effect, as well as the absolute interaction effect of two or more factors.

The effect of each factor and the interaction effect of two or more factors are defined by considering the *Statistical Analysis of the t-test*, also known as *Signal-to-Noise* test. This test computes the ratio between the difference of the means of the response and the *standard error of the difference*. In the current analysis the difference between the maximum and minimum means are considered. Hence:

$$\begin{cases} X_i = (av_{i,+}, av_{i,-})_{max} - (av_{i,+}, av_{i,-})_{min} & \text{if two level factor} \\ X_i = (av_{i,+}, av_{i,0}, av_{i,-})_{max} - (av_{i,+}, av_{i,0}, av_{i,-})_{min} & \text{if three level factor} \end{cases} \tag{4.2.1}$$

Where

$av_{i,+}$, $av_{i,0}$ and $av_{i,-}$ are the average responses of the ith factor at the *High*, *Zero* and *Low* levels.

The formula defining the t value is:

$$t = \frac{X_i}{\sqrt{\frac{\sigma^2_{i,max}}{n_{i,max}} + \frac{\sigma^2_{i,min}}{n_{i,min}}}}$$

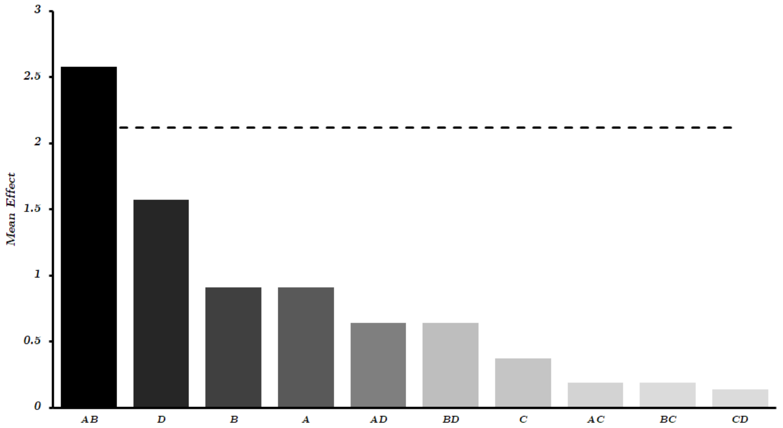

Figure 4.6: Pareto general chart of the main and interaction effects on γ; A: Rail Gauge B: Wheelset design C: Vertical Railpad stiffness D: Vertical Ballast stiffness

where $\sigma_{i,max}$ is the variance of the response of the ith factor for the maximum case, $\sigma_{i,min}$ is the variance of the response of the ith factor for the minimum case, $n_{i,max}$ is the number of samples for the maximum case and $n_{i,min}$ is the number of samples for the minimum case.

The t value is also called *standardized effect* and can be computed automatically by most statistical software. In this analysis, MINITAB has been used to perform the necessary numerical evaluations.

To test the significance, a set risk level called *alpha level* has to be chosen. Typically, an alpha level of 0.05 is used. Also, the degrees of freedom (df) for the test has to be determined. It can be computed as:

$$df = n_{i,max} + n_{i,min} - 2$$

Given the alpha level and the df, one can compute the necessary t value in order to have statistical significance by using commonly used t distribution tables [41].

Figure 4.6 depicts the Pareto chart of standardized effects. In the analysis, both main effects and interaction effects up to the second order interactions are considered. The dashed line represents the significance level with an alpha level of 0.05.

Here again, one can detect the global great influence of the interaction effect between gauge and wheelset design. Moreover, the interaction effect of wheelset design and the gauge is the only significant factor in the analysis at 95% of confidence.

4.3 Single factors effect

In order to analyze the effect that factors that are not considered in the design of experiments have on the corrugation index, a single run case taken from the analysis is considered as a study model. In detail, the run case *2-4* of the design of experiments has been considered as a study model.

Two additional parameters have been analyzed, that are:

- Friction coefficient
- Rail pad vertical damping

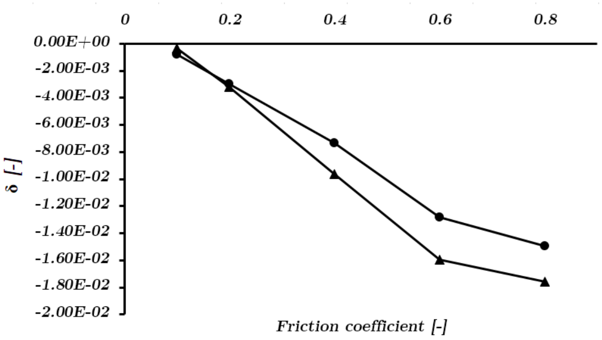

Figure 4.7: Case *2-4*: Effect of the friction coefficient μ on the effective damping ratio ●: I mode; ▲ II mode

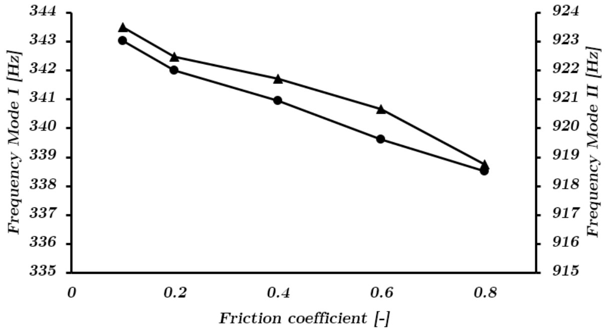

Figure 4.8: Case *2-4*: Effect of the friction coefficient μ on the frequency of unstable vibration ●: I mode; ▲ II mode

4.3.1 Friction Coefficient

The wheel-rail friction coefficient plays a fundamental role in the definition of the magnitude of the contact forces. The relation between the magnitude of the tangential contact forces and friction coefficient is linear (see Eq. 2.5.3). It is interesting to check if the relation between friction coefficient and the corrugation occurrence follows the same trend.

Figure 4.7 shows the effect of the friction coefficient on the effective damping ratio of the unstable modes. As expected, the effective damping ratio magnitude increases linearly with respect to the friction coefficient.

Figure 4.8 shows the effect of the friction coefficient on the frequency of the unstable modes. Interestingly, the relationship is characterized by a distinct linear shift of the frequencies of both unstable modes at a lower range for bigger friction coefficient values.

4.3.2 Vertical RailPad Damping

The same procedure has been conducted in order to analyze the effect of the vertical rail pad damping on the corrugation occurrence.

Figure 4.9 shows the effect of the vertical rail pad damping on the effective damping

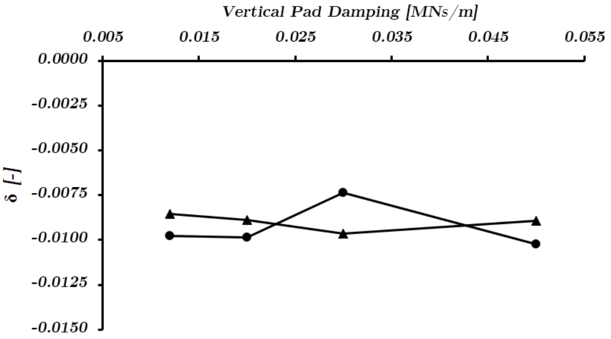

Figure 4.9: Case *2-4*: Effect of the vertical railpad damping on the effective damping ratio ●: I mode; ▲ II mode

ratio of the unstable modes. No correlation can be evidenced. One can conclude that:

- By considering the structural parameters defining the run case 2-4, *there is no correlation between the vertical rail pad damping and corrugation formation.*

There might still be interaction effects between this factor and other structural factors. However, this aspect has not been tackled in the thesis.

Chapter 5

Summary and Conclusions

In this Chapter, a brief summary of the project and an organization of the main significant results will be lined up. Moreover, a brief description of the limitations of the work and the suggestions for further research on the topic will be discussed.

5.1 Summary

This thesis work focused on the still open research problem of rail corrugation, aiming at finding novel practices for preventing this phenomenon from occurring. The project has been preventively decided to be developed by relying on the relatively recent theory, by Chen et al., based on considering the *self-excited vibrations* of the leading wheelset as the main wavelength-fixing mechanism on rail corrugation. This work aimed at expanding the literature knowledge on this approach by critically using it as a reference.

The approach used in this research was to build a 3D finite elements model, developed by using the computer software ABAQUS, to predict the self-excited vibrations of the coupled leading wheelset-rail track system caused by some form of instability induced by the wheel-rail contact forces. The wheelset, sleepers, and rails were modeled in ABAQUS as elastic bodies by using brick elements and linear elastic material properties. Ballast and rail pads were modeled by deploying spring-dashpots systems in parallel characterized linear properties. The friction contact model employed was a simplified model that considers a classical Coulomb friction model for a sufficiently high total contact slip, and an elastic slip for small values of contact slip.

The model built was then validated against the available results of the published literature used as the reference. Using the validated ABAQUS model, a series of analyses concerning the variation of the instability of the system against several geometrical-structural factors were conducted.

5.2 Conclusions

The model validation procedure showed that the finite elements model developed is able to accurately predict the same results of the published works taken as reference. Since the models have two distinct rail lengths, a first simple yet significant conclusion is:

- *For the purpose of the study of rail corrugation in curved tracks through the employment of a self-excited vibration detection model, it is sufficient to use a rail length of 11.4 meters instead of the standard 36 meters commonly used for dynamic analyses.*

This fact is related to the observation that the rails are only marginally affected by the unstable vibration: most of the vibration is related to the leading wheelset body. This conclusion leads to the practical outcome of a way lighter computational effort for performing the same analysis. Naturally, this conclusion is valid only for the application considered in this thesis.

Another point to be stressed is the number of results that match with the experimental pieces of evidence about rutting corrugation. Firstly:

- *The unstable modes detected in the analysis have always most of the vibration displacement on the low rail side wheel.*

This is in good agreement with the evidence that rutting corrugation in tight curved tracks is almost always formed at the low rail. Secondly:

- *85% of the unstable cases have the most unstable mode at a frequency between 340 and 495 Hz, which is a typical rutting fixing frequency.*
- The relation between rail pad stiffness and corrugation formation, according to the theory used, leads to a *lower corrugation formation for softer rail pads*, which is another typical literature result.

These results taken alone give a faint credit to the correlation between *self-excited vibrations* and rail corrugation at curved rail tracks.

The design of experiments analysis showed that :

- *There is a strong influence on rail corrugation of the interaction effect of rail gauge and the wheelset design*

This last conclusion might be the most interesting of the thesis since this means that the gauge widening used in correspondence of tight curves might have a strong influence on the wheelset stability. Nevertheless, rail gauge can be more seen as a *co-factor*, since its value is firmly defined by standards and more important aspects than the corrugation formation, e.g. bogie dynamics in curved tracks. However, on the other side, this conclusion equally states that the wheelset geometry, besides of the expected unstable mode frequency influence affects also the stability of the wheelset at a particular gauge value. This leads to the implication that, if the self-excited vibrations theory on rail corrugation is valid, the wheelset geometry can be considered in the corrugation optimization analysis as one potential inhibitor factor.

Moreover, the analysis of the effect of the friction coefficient on the wheelset stability showed that:

- *For higher friction coefficient values, the frequency of unstable vibration gets smaller*

This is an interesting conclusion, explained by the fact that the contribution of the friction coefficient on the stiffness matrix of the system is negative.

5.3 Limitations of the study

The analysis of this thesis is limited to wheel and rail profiles typically used in principal networks; therefore, it hasn't been considered *light rail* corrugation, which can have different causes. Moreover, the loads considered at the wheelset bearings, and the suspensions parameters are typical of passenger transportation applications. Therefore, the study doesn't include corrugation induced by freight trains. Finally, the analysis is limited to the case of corrugation formed at tight curves; therefore, it hasn't been considered the case of corrugation formed on straight tracks.

5.4 Future work

The research in this thesis has pointed out the potential reliability of the *self-excited vibrations* theory on rail corrugation and, under this hypothesis, it is demonstrated that the interaction effect of rail gauge and wheelset design has a strong influence on rail corrugation. However, the conclusions of the thesis rely on the self-excited vibrations theory on rail corrugation. The best approach to validate the theory would be to perform experimental evaluations. Nevertheless, additional studies on the influence on the wheelset stability of wheelset geometrical factors could give more detailed pieces of information about the way the wheelset design affects the wheelset stability at a given rail gauge, giving more in-depth conclusions. Additional studies that investigate the conclusions of this thesis by means of different numerical approaches would make them more solid and give more credit to the used theory.

Bibliography

[1] J. Alias (1986), *"Characteristics of wave formation in rails"*

[2] K.H. Oostermeijer (2008), *"Review on short pitch rail corrugation studies"*

[3] E.G. Vadillo, J.A. Tarrago, G.G. Zubiaurre, C.A. Duque (1997), *Effect of sleeper distance on rail corrugation*

[4] S.L. Grassie, J.A. Elkins (2007), *"Rail Corrugation on north american transit systems"*

[5] RailMeasurement Ltd (2015), *railmeasurement.com*

[6] S.L. Grassie, J. Kalousek (1993), *"Rail Corrugation: characteristics, causes, and treatments"*

[7] A. Kapoor, F.J. Franklin, S.K. Wong, M. Ishida (2002), *Surface roughness and plastic flow in rail wheel contact*

[8] S.L. Grassie (2009), *"Rail Corrugation: characteristics, causes, and treatments"*

[9] Simon Iwnicki (2006), *"Handbook of Railway Vehicle Dynamics"*

[10] W.J. Qian, G.X. Chen, H. Ouyang, M.H. Zhu, W.H. Zhang, Z.R. Zhou (2014), *"A transient dynamic study of the self-excited vibration of a railway wheelset-track system induced by saturated creep forces"*

[11] Y.Q. Sun, S. Simon (2008), *Wagon-track modelling and parametric study on rail corrugation initiation due to wheel stick-slip process on curved track*

[12] A. Matsumoto, Y. Sato, H. Ono, M. Tanimoto, Y. Oka, E. Miyauchi (2002), *Formation mechanism and countermeasures of rail corrugation on curved track*

[13] Simon Iwnicki (2006), *"Handbook of Railway Vehicle Dynamics"*

[14] Coenraad Esveld (2001), *"Modern railway Track, Second Edition"*

[15] Andreas Carlberger (2016), *"Simulation of Rail Corrugation Growth on Curves"*

[16] Zhihui Zhu; Michael T. Davidson, M.ASCE; Issam E. Harik, M.ASCE; and Yu Zhi-wu (2017), *"Train-Induced Vibration Characteristics of an Integrated High-Speed Railway Station"*

[17] N. Bosso et al. (2013), *"Mechatronic Modeling of Real-Time Wheel-Rail Contact"*

[18] T Tinga (2013), *"Principles of Loads and Failure Mechanisms: Applications in Maintenance"*

[19] H. Hertz (1881), *"Über die Berührung fester elastischer Körper, Journal für die reine und angewandte Mathematik 92"*

[20] J. J. Kalker (1991), *"Wheel-rail rolling contact theory"*

[21] ABAQUS Inc. (2016), *"Abaqus Analysis User's Manual, Version 6.14."*

[22] J.F. Archard (1953), *"Contact and Rubbing of Flat Surfaces," Journal of Applied Physics, Vol.24, pp.981-988*

[23] M. Nouby, D. Mathivanan, K.Srinivasan (2009), *A combined approach of complex eigenvalue analysis and design of experiments (DOE) to study disc brake squeal*

[24] A.R. AbuBakar, H. Ouyang (2006), *Complex eigenvalue analysis and dynamic transient analysis in predicting disc brake squeal*

[25] A.R. AbuBakar, M. K. A. Hamid, A. Dzakaria, B. A. Ghani, M. Mohamad (2006), *Stability analysis of disc brake squeal considering temperature effect*

[26] P. Liu, H. Zheng, C. Cai, Y.Y. Wang, C.Lu, K.H. Ang, G.R. Liu (2007), *Analysis of disc brake squeal using the complex eigenvalue method*

[27] G.X. Chen, Z.R. Zhou, H. Ouyang, X.S. Jin, M.H. Zhu, Q.Y. Liu *A finite element study on rail corrugation based on saturation creep force-induced self-excited vibration of a wheelset-track system*

[28] X.L.Cui, G.X. Chen, H.G. Yang, Q.Zhang, H.Quyang & M.H. Zhu (2016) *Study on rail corrugation of a metro tangential track with Cologne-egg type fasteners*

[29] B.C Goo, J.C. Kim (2016), *"Complex eigenvalue analysis of railway wheel/rail squeal"*

[30] European committee for standardization (2003), *EN13674*

[31] G. Mastinu (2016), *"Ground Vehicle Engineering course notes"*

[32] trv.jbv.no (2017), *"Pandrol Fastclip FE; Tegning: OB 800136 "*

[33] European committee for standardization (2003), *prEN 13715 - Railway applications- Wheelsets and bogies - Wheels- Tread profile*

[34] M. Oregui, Z. Li, R. Dollevoet (2014), *An investigation into the modeling of railway fastening*

[35] NIST (2013), *itl.nist.gov*

[36] H. Ilias (1998), *The influence of railpad stiffness on wheelset/track interaction and corrugation growth*

[37] J.I. Egana, J. Vinolas, M. Seco (2005), *Investigation of the influence of rail pad stiffness on rail corrugation on a transit system*

[38] S. Leonardi, *Corso di Infrastrutture Aeroportuali, Ferroviarie ed Intermodali*

[39] Kl. Knothe, S.L. Grassie, *Modelling of Railway Track and Vehicle/Track Interaction at High Frequencies*

[40] J.P. Huille (1992), *EUropean Research project for Optimised BALiasted Tracks*

[41] William M.K. Trochim (2006), *socialresearchmethods.net*

Appendix A

Analysis input script *(2-4)*

```
** BOUNDARY CONDITIONS
**
** Name: Bearings BCs Type: Displacement/Rotation
*Boundary
Set-867, 3, 3
Set-867, 4, 4
Set-867, 5, 5
Set-867, 6, 6
** Name: Rail BCs Type: Symmetry/Antisymmetry/Encastre
*Boundary
Set-1141, PINNED
**
** INTERACTIONS
**
** Interaction: High Rail
*Contact Pair, interaction=”Contact Model”, type=SURFACE TO SURFACE, adjust=0.0
s-Surf-94, m-Surf-94
** Interaction: Low Rail inside
*Contact Pair, interaction=”Contact Model”, type=SURFACE TO SURFACE, adjust=0.0
s-Surf-96, m-Surf-37
** ----------------------------------------------------------------
**
** STEP: Contact Initiation
**
*Step, name=”Contact Initiation”, nlgeom=YES
*Static
0.02, 0.1, 1e-06, 0.1
**
** BOUNDARY CONDITIONS
**
** Name: Contact initiation Type: Displacement/Rotation
*Boundary
Set-868, 1, 1, 3.
```

```
Set-868, 2, 2, -4.
**
** OUTPUT REQUESTS
**
*Restart, write, frequency=0
**
** FIELD OUTPUT: F-Output-1
**
*Output, field
*Node Output, exterior
CF, RF, RT, U
*Element Output, exterior, directions=YES
S,
*Contact Output
CFORCE, CSTATUS, CSTRESS
**
** HISTORY OUTPUT: H-Output-1
**
*Output, history
*Contact Output
CFN1, CFN2, CFN3, CFNM, CFS1, CFS2, CFS3, CFSM
*End Step
** ————————————————————————-
**
** STEP: Suspension forces initiation
**
*Step, name=”Suspension forces initiation”, nlgeom=YES
*Static
0.01, 0.1, 1e-06, 0.1
**
** BOUNDARY CONDITIONS
**
** Name: Bearings BCs Type: Displacement/Rotation
*Boundary, op=NEW
Set-867, 3, 3
Set-867, 4, 4
Set-867, 5, 5
Set-867, 6, 6
** Name: Contact initiation Type: Displacement/Rotation
*Boundary, op=NEW
Set-868, 1, 1, 3.
** Name: Rail BCs Type: Symmetry/Antisymmetry/Encastre
*Boundary, op=NEW
Set-1141, PINNED
**
** LOADS
**
** Name: High Vertical Suspension Force Type: Concentrated force
*Cload
Set-870, 1, 0.
```

```
Set-870, 2, -80000.
** Name: Low Vertical Suspension Force Type: Concentrated force
*Cload
Set-869, 1, 0.
Set-869, 2, -85900.
**
** OUTPUT REQUESTS
**
*Restart, write, frequency=0
**
** FIELD OUTPUT: F-Output-1
**
*Output, field, frequency=99999
*Node Output, exterior
CF, RF, RT, U
*Element Output, exterior, directions=YES
S,
*Contact Output
CFORCE, CSTATUS, CSTRESS
**
** HISTORY OUTPUT: H-Output-1
**
*Output, history
*Contact Output
CFN1, CFN2, CFN3, CFNM, CFS1, CFS2, CFS3, CFSM
*End Step
** ----------------------------------------------------------------
**
** STEP: Suspension forces initiation 2
**
*Step, name=”Suspension forces initiation 2”, nlgeom=YES
*Static
0.01, 0.1, 1e-06, 0.1
**
** BOUNDARY CONDITIONS
**
** Name: Bearings BCs Type: Displacement/Rotation
*Boundary, op=NEW
Set-867, 3, 3
Set-867, 4, 4
Set-867, 5, 5
Set-867, 6, 6
** Name: Contact initiation Type: Displacement/Rotation
*Boundary, op=NEW
** Name: Rail BCs Type: Symmetry/Antisymmetry/Encastre
*Boundary, op=NEW
Set-1141, PINNED
**
** LOADS
**
```

```
** Name: High Vertical Suspension Force Type: Concentrated force
*Cload
Set-870, 1, 523.
** Name: Low Vertical Suspension Force Type: Concentrated force
*Cload
Set-869, 1, 7400.
**
** OUTPUT REQUESTS
**
*Restart, write, frequency=0
**
** FIELD OUTPUT: F-Output-1
**
*Output, field, frequency=99999
*Node Output, exterior
CF, RF, RT, U
*Element Output, exterior, directions=YES
S,
*Contact Output
CFORCE, CSTATUS, CSTRESS
**
** HISTORY OUTPUT: H-Output-1
**
*Output, history
*Contact Output
CFN1, CFN2, CFN3, CFNM, CFS1, CFS2, CFS3, CFSM
*End Step
** ————————————————————————————-
**
** STEP: Sliding initiation
**
*Step, name=”Sliding initiation”, nlgeom=YES
*Static
0.005, 0.1, 1e-06, 0.1
*MOTION, TRANSLATION, TYPE=VELOCITY
Wheelset, 1,2, -88.70,-5.876
**
** BOUNDARY CONDITIONS
**
** Name: Bearings BCs Deformed shape Type: Velocity/Angular velocity
*Boundary, type=VELOCITY
Set-993, 1, 1
Set-993, 2, 2
**
** OUTPUT REQUESTS
**
*Restart, write, frequency=0
**
** FIELD OUTPUT: F-Output-1
**
```

```
*Output, field, frequency=99999
*Node Output, exterior
CF, RF, RT, U
*Element Output, exterior, directions=YES
S,
*Contact Output
CFORCE, CSTATUS, CSTRESS
**
** HISTORY OUTPUT: H-Output-1
**
*Output, history
*Contact Output
CFN1, CFN2, CFN3, CFNM, CFS1, CFS2, CFS3, CFSM
*End Step
** ----------------------------------------------------------------
**
** STEP: Natural frequencies extraction
**
*Step, name=”Natural frequencies extraction”, perturbation
*Frequency, eigensolver=Lanczos, sim, acoustic coupling=projection, normalization=mass
1500, 0.1, 1300., , ,
**
** OUTPUT REQUESTS
**
*Restart, write, frequency=0
**
** FIELD OUTPUT: F-Output-2
**
*Output, field
*Node Output, exterior, variable=PRESELECT
*Element Output, exterior, directions=YES, variable=PRESELECT
*Energy Output, variable=PRESELECT
*Contact Output, variable=PRESELECT
*End Step
** ----------------------------------------------------------------
**
** STEP: CE Analysis
**
*Step, name=”CE Analysis”, perturbation, unsymm=YES
*Complex Frequency, friction damping=NO
1200, 0.5, 1000.,
**
** OUTPUT REQUESTS
**
**
** FIELD OUTPUT: F-Output-3
**
*Output, field
*Node Output, exterior, variable=PRESELECT
*Element Output, exterior, directions=YES, variable=PRESELECT
```

```
*Energy Output, variable=PRESELECT
*Contact Output, variable=PRESELECT
*End Step
```